FLOOD INUNDATION MAPPING USING RRI MODEL FOR KULSI RIVER BASIN (ASSAM/MEGHALAYA)

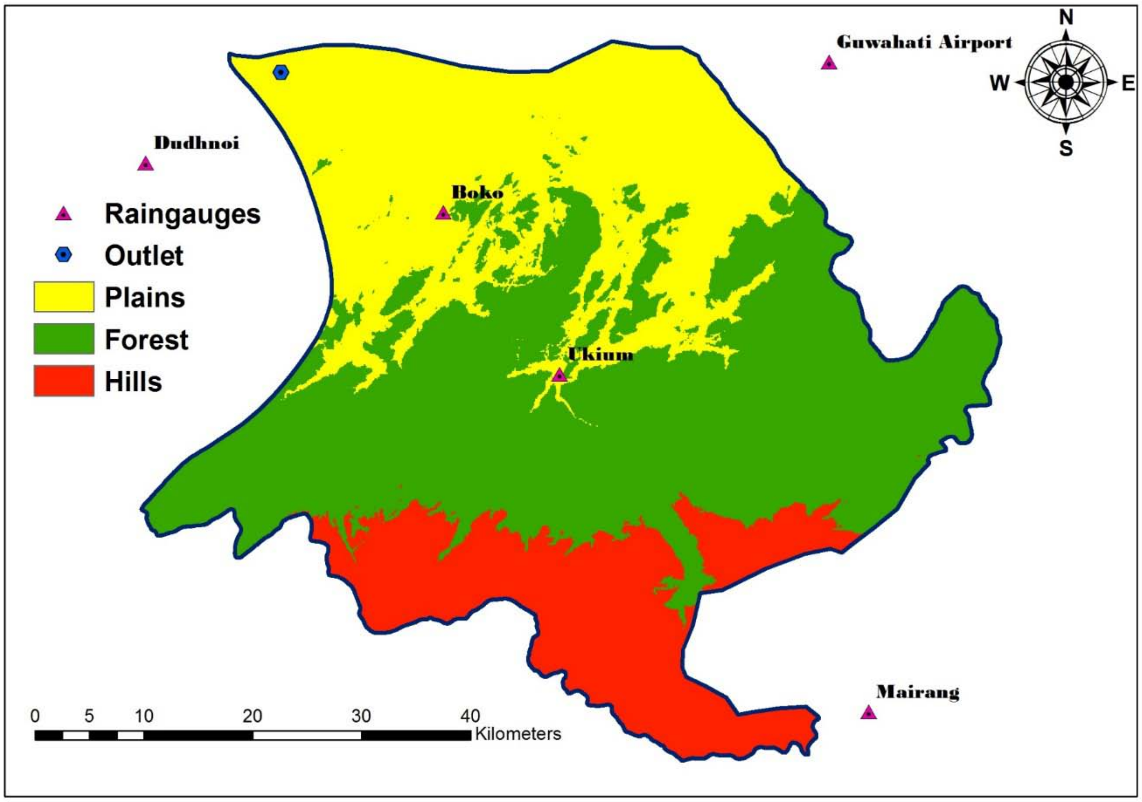

NATIONAL INSTITUTE OF HYDROLOGY
Centre for Flood Management Studies
Dispur, Guwahati – 781 006
2015-16

PREFACE

IWRM is a process which promotes the coordinated development and management of water, land and related resources (Global Water Partnership, 2000). Keeping in view the importance of IWRM, National Institute of Hydrology (NIH), a premier Institute in the area of hydrology and water resources in India, set up regional centers for taking up studies relating to the field problems and also to develop closer interaction with the water resources organizations in different regions of the country.One such regional center was set up at Guwahati for the North-Eastern Regioncatering for the various water resources problems of seven North East States, Sikkim and parts of West Bengal.

Considering flood as the major problem in the region, Ministry of Water Resources, Govt. of India decided to rededicate the Regional Centre towards service of the region and renamed it as NIH Centre for Flood Management Studies for the Brahmaputra Basin (NIH-CFMS).Under the mandate of XII plan period, the center is working on a project in IWRM under Pilot Basin Study (PBS). The PBS program involves identification of suitable basin in consultation with concerned State Govt. authorities, establishment of advanced instrumentation for data collection and storage, data processing and analysis using state of the art models, preparation of results and findings in collaboration with specialists of other relevant disciplines in a meaningful and usable form for the intended beneficiaries and stake holders.

The Kulsi River Basin, a part of the Brahmaputra sub-basin, situated on the south bank of the mighty River Brahmaputra was identified for PBS study. The basin spreads in the Kamrup District of Assam as well as west Khasi hills and Ribhoi district of Meghalaya. The river Kulsi drains out a total area of 2806 sq. km. within the Kamrup District of Assam as well as west Khasi hills and Ri Bhoi district of Meghalaya.The selected basin is ideal to develop flood inundation maps due to its strategic location encompassing two states in the north-east coupled with the fact that the region experiences maximum floods.

Most of the basins in North East India have insufficient hydrological gauge stations, which makes the reliance on availability of satellite products even more important for hydrologic simulations. The importance of topography has been highlighted in the previous section. Elevation data from different sources are widely available even for data-poor developing country. This study focuses their effect on floods simulations. DEM preprocessing plays an important role in final simulations and the impact of DEM smoothing on flood inundation mapping is considered in this study.

The report has been prepared by Dr. Sanjay Kumar Sharma, Sc. ‘B’, Er. Gulshan Tirkey, Sc ‘B’ and Dr. C. K. Jain, Sc ‘G’ & Head/ Coordinator, Centre for Flood Management Studies, Guwahati, under the work programme for 2015-16.

(R. D. Singh)
Director

CONTENTS

LIST OF FIGURES

LIST OF TABLES

LIST OF ABBREVIATIONS

ASMF	Adaptive Spectral Median Filter
ASTER	Advanced Spaceborne Thermal Emission and Reflection Radiometer
CARTO	CARTOSAT-1
CFMS	Centre for Flood Management Studies
CSI	Critical Success Index
DEM	Digital Elevation Model
GPS	Global Positioning System
ED	Elevation Difference
FAO	Food and Agriculture Organization
GCF	Gaussian Cut Filter
GCP	Ground Control Point
GWP	Global Water Partnership
ISRO	Indian Space Research Organisation
IWRM	Integrated Water Resources Management
MAE	Mean Absolute Error
MCF	Mean Curvature Flow
METI	Ministry of Economy, Trade and Industry, Japan
MLSWI	Modified Land Surface Water Index
MODIS	Moderate resolution Imaging Spectoraradiometer
NASA	National Aeronautics and Space Administration, USA
NIR	Near Infra-Red
NSE	Nash-Sutcliffe Coefficient of Efficiency
PBS	Pilot Basin Study
RMSE	Root Mean Square Error
RRI	Rainfall-Runoff-Inundation
r	Coefficient of correlation
SRTM	Shuttle Radar Topography Mission
SWIR	Short Wave Infra-Red

ABSTRACT

Topography affects different aspects of the water balance in a catchment. Different sources of Digital Elevation Model (DEM) characterizing the topography are available online and their suitability for hydrologic simulation needs to be accessed. The removal of noise from DEM using smoothing filters also influences spatial distribution of flood inundation mapping needs to be quantified.

Centre for Flood Management Studies, National Institute of Hydrology, India has identified Kulsi River Basin for undertaking Pilot Basin Study (PBS) as a component of Integrated Water Resource Management (IWRM). The basin has experienced severe flooding in 2007 and 2008. Rainfall-Runoff-Inundation (RRI) hydrological model was used in this study to simulate discharge and inundation extent for the flood events. The objectives of the study were a) to evaluate the sensitivity on hydrologic simulation using SRTM (Shuttle Radar Topography Mission), ASTER (Advanced Spaceborne Thermal Emission and Reflection Radiometer) and CARTO (CARTOSAT-1) DEM and b) to evaluate the impact of smoothing of DEM using low pass filter, enhanced lee filter (window size 3 and 5) and denoising filters o on discharge and flood inundation extent. Result of flood area from RRI were verified with flood extent from MODIS derived Modified Land Surface Water Index (MLSWI).

Sensitivity analysis showed that RRI Model is highly sensitive to Manning’s roughness coefficient values for flood plain, followed with source of DEM and then soil depth among the input parameters. The simulated inundation extent was found to be more influent by smoothing filters than its simulated discharge at the outlet. RRI model simulations of discharge and inundation area showed good agreement with the MODIS derived flood extents. Combination of ASTER DEM with denoising algorithm performed better hydrologic simulations of discharge and inundation extent among all other input combinations for Kulsi River Basin.

Keywords: DEM, SENSITIVITY, FILTERING, RRI, MODIS

1. INTRODUCTION

1.1 Background

Asia is the world's most disaster-prone region, registering the largest number of people affected, as well as death toll by disasters (UNESCAP, 2013). India on account of its geographical position, climate and geological setting, is highly vulnerable to natural hazards such as cyclone, drought, floods, earthquakes, fire, landslides and avalanches. Floods are the most common natural disaster which occurred in India between the period of 1980-2010 (UNISDR, 2012), as shown in Figure 1.1.

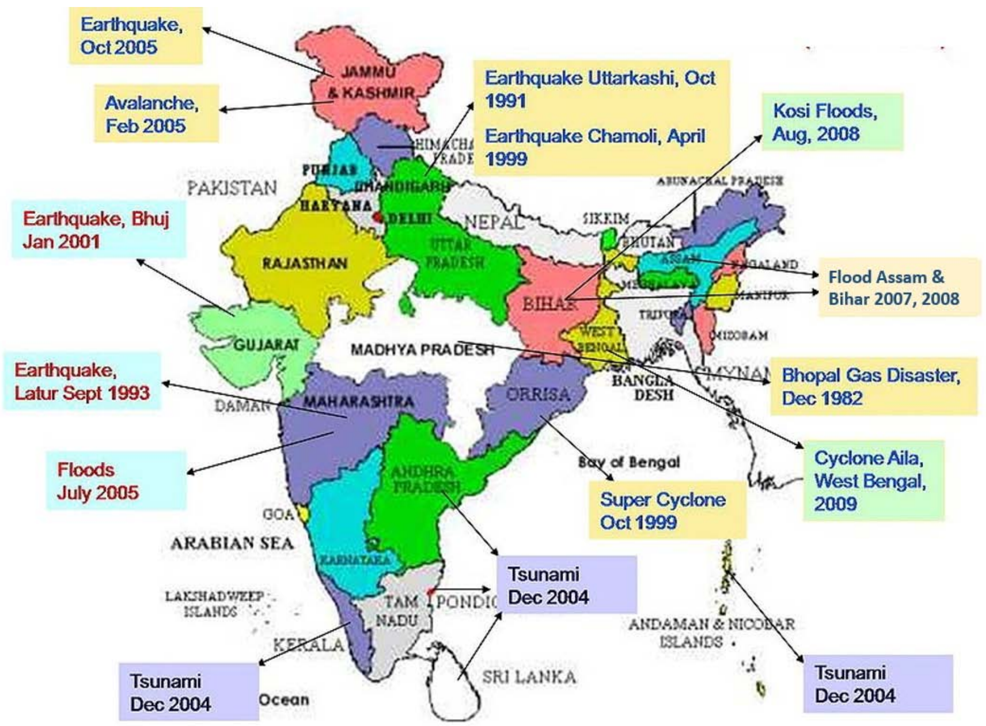

Fig 1.1 Major disaster in India (1980-2010)

Source: UNISDR, 2012

The most flood prone areas in India are the Brahmaputra and Ganga River basins in the Indo-Gangetic-Brahmaputra plains in North and Northeast India, which carry 60 per cent of the nation's total river flow (Singh et al., 2008). With 40% of its land surface susceptible to flood damage, Assam's Brahmaputra valley represents one of the most acutely hazard-prone regions in the country, having a total flood-prone area of 3.2 million ha. (Goswami and Das, 2003). Floods in Assam are caused by a combination of natural and anthropogenic factors. The unique geo-environmental setting of the basin consisting of the eastern Himalayas, the highly potent monsoon regime, weak geological formation, active seismicity, accelerated erosion, rapid channel aggradation, massive deforestation, intense land-use pressure and high population growth, especially in the floodplain belt and ad hoc temporary flood control measures are some of the dominant factors that cause and/or intensify floods in Assam. The scenario is further exacerbated by a myriad of social, environmental and economic factors that make populations increasingly vulnerable (Goswami, 2008).

The management of floods as problems in isolation results in a piecemeal, localized approach. Integrated Water Resources Management (IWRM) calls for a paradigm shift from the traditional fragmented approach, and encourages the efficient use of the resources of the river basin as a whole, employing strategies to maintain or augment the productivity of floodplains, while at the same time providing protective measures against the losses due to flooding (Global Water Partnership, 1999). Identification of areas affected by floods is an important input for devising the strategy for efficient management of floods.

The severity and scale of flood management measures depends upon the magnitude of flood prone areas and frequency of occurrence of flooding in the area. Rashtriya Barh Ayog (Central Water Commission, 1996) highlighted the concern about the authenticity of flood prone area figures reported by some of the states. The expert group has suggested a scientific approach to identify the flood prone areas. Floodplain zoning is a procedure used to identify areas of varying flood hazard and has been used extensively as a precursor to land use regulation, a non-structural floodplain management measure. The general terminologies of various types of maps prepared for flood plain zoning and their brief descriptions are given below (Hewitt, 1997,Varley, 1994 and Mitchell, 1999).

Flood inundation map: A flood inundation map provides information about areal extent of inundation for a reach of a river during a flood event when the flood water in the river overtops its banks and leads to the flooding of adjoining areas or flood plains. The flood inundation map for a reach of river may be prepared by demarcation with physical inputs i.e. by demarcating the various locations of the flood plains which get inundated during a particular flood. Alternatively, such flood inundation maps may also be prepared using remote sensing data pertaining to the flood period and the reach of the river.

Flood hazard map: A flood hazard map provides information about return period associated with the areal extent of inundation for a reach of a river. The flood hazard maps are prepared delineating areas subjected to inundation by floods of various magnitudes and frequencies. These maps serve as important tools in proper flood plain management. Figure 1.2 shows the flood hazard map of India obtained from Vulnerability Atlas of India (BMPTC, 1997).

Flood risk map: A flood risk map provides information about risk associated with the damages caused or losses resulting from a flood event in a particular area or flood risk. Preparation of flood risk map incorporates the financial aspects and provides the actuarial inputs for flood insurance plans and for other purposes.

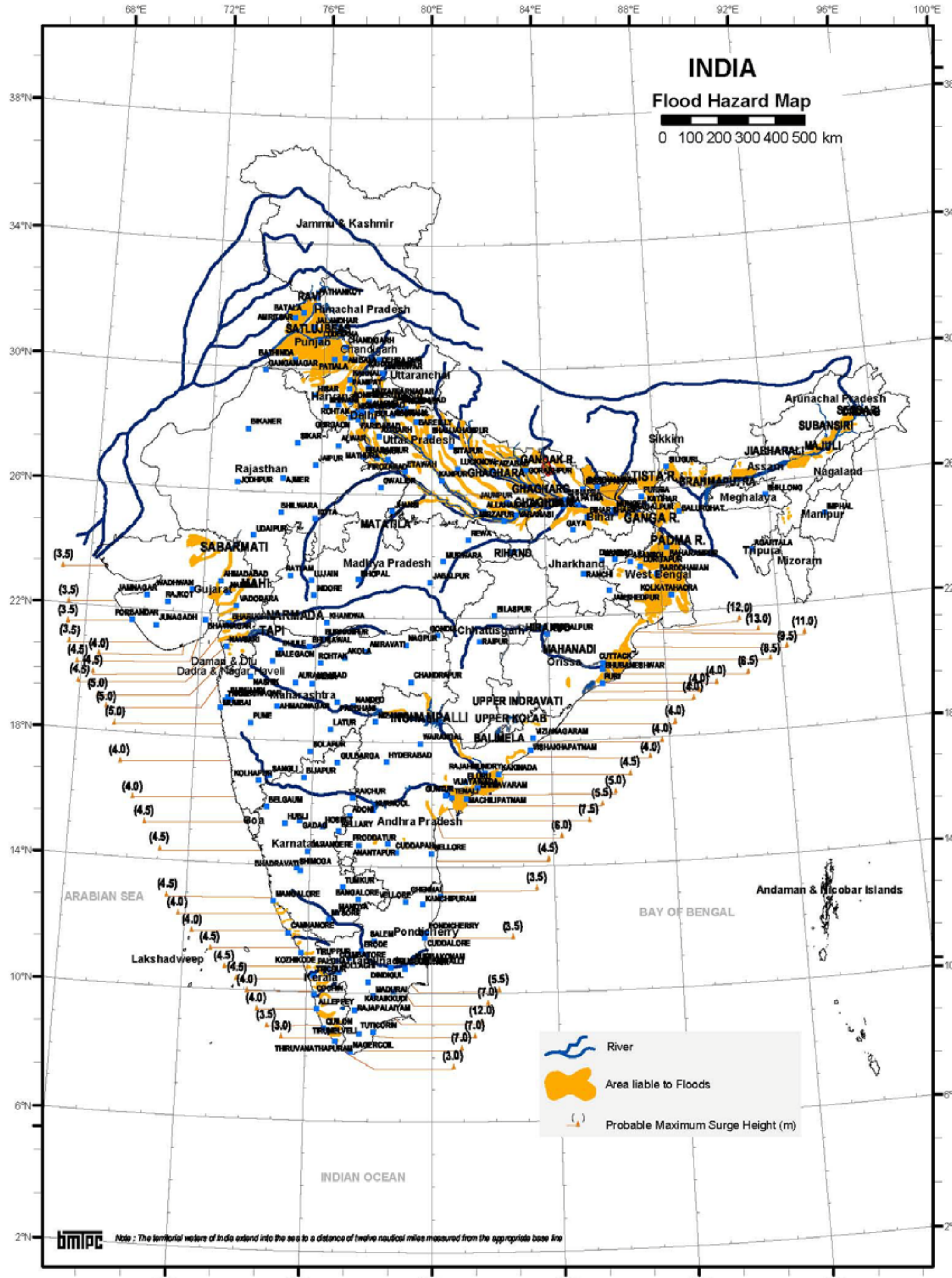

BMTPC : Vulnerability Atlas -2nd Edition; Peer Group, MoH&UPA; Map is Based on digitised data of SOI, GOI; Flood Atlas, Task Force Report, C.W.C., G.O.I.

Figure 1.2 Flood hazard map of India

(Source: BMPTC, 1997)

1.2 Importance of topography in flood inundation mapping

Topography is an important land-surface characteristic that affects most aspects of the water flow in a catchment, including the generation of surface and sub-surface runoff; the flow paths followed by water as it moves down and through hill slope and the rate of water movement. All of the distributed hydraulic and hydrological models use topography to derive bathymetry. Topographic data affect hydraulic simulations through geometric description which defines the domain for performing numerical computations in a model. Topography plays a major role in determining the accuracy of hydraulic modelling and flood inundation mapping (Brandt, 2005, Cook and Merwade, 2009). Manfreda et al. (2008) investigated the topographic attributes of the terrain and observed a strong correlation between the topographic index (Kirkby, 1975) and areas exposed to flood inundation. In particular, flood-prone areas were found to be characterized by high topographic convergence (high topographic index). The topographic index was found to be well correlated with the areas where meteoric water tends to accumulate (e.g., Beven and Kirkby 1979; Western et al. 2002), it is likely that this is also indicative of areas most exposed to flood inundation.

Digital Elevation Model (DEM) is a raster dataset containing information about the topography of a region and is used as a prerequisite to hydraulic modelling. For hydraulic modelling purposes, DEM are used to determine the active channel cross-sectional elevations, water surface elevations and flood extents. Resolution and accuracy are the two main properties of a DEM that affect hydraulic and hydrologic modelling results (Vaze et al., 2010). DEM can be acquired from many sources of topographic information ranging from the high-resolution and accurate, but costly, LIDAR (Light Detection and Ranging) obtained from lower altitude, to low-cost, and coarse resolution, spaceborne data, such as ASTER (Advanced Spaceborne Thermal Emission and Reflection Radiometer), SRTM (Shuttle Radar Topography Mission) and The Cartosat-1 Digital Elevation Model (CARTO DEM). Considerable variation is observed among the different DEM spatial resolution, vertical precision and accuracy. This diversity is caused by the types of equipment and methods used in obtaining the topographic data. When used as an input to hydraulic modelling, the differences in the quality of each DEM subsequently result in differences in model output performance. The usefulness of diverse topographic data in supporting hydraulic modelling of floods is subject to the availability of DEM, economic factors and geographical conditions of survey area. To date, many studies have been carried out with the aim of evaluating the impact of accuracy and precision of the topographic data on the results of hydraulic models (Cobby and Mason, 1999; Casas et al., 2006; Schumann et al., 2008)

Casas et al. (2006) investigated the effects of the topographic data sources and resolution on 1-D hydraulic modelling of floods. They found that the contour-based DEM was the least accurate in the determination of the water level and inundated area of the floodplain; however, the GPS-based DEM led to a more realistic estimate of the water surface elevation and of the flooded area.

Schumann et al. (2008) demonstrated the effects of DEM on deriving the water stage and inundation area. Three DEM at three different resolutions from three sources (LIDAR, contour and SRTM DEM) were used for a study area in Luxembourg. By using the HEC-RAS 1-D hydraulic model to simulate the flood propagation, the result shows that the LIDAR DEM derived water stages by displaying the lowest RMSE, followed by the contour DEM and lastly the SRTM. Considering the performance of the SRTM, they suggested that the SRTM DEM is a valuable source for initial vital flood information extraction in large, homogeneous floodplains.

For the large flood-prone area, the availability of DEM from the public domain (e.g. ASTER, SRTM) makes it easier to conduct a study. Patro et al. (2009) selected a study area in India and demonstrated the usefulness of using SRTM DEM to derive river cross-section for the use in hydraulic modelling. They found that the calibration and validation results from the hydraulic model performed quite satisfactorily in simulating the river flow. Furthermore, the model performed quite well in simulating the peak flow, which is important in flood modelling.

The study by Tarekegn et al. (2010) carried out on a study area in Ethiopia used a DEM which was generated from ASTER image. Integration between remote sensing and GIS technique were needed to construct the floodplain terrain and channel bathymetry. From the results obtained, they concluded that the ASTER DEM was able to simulate the observed flooding pattern and inundated area extents with reasonable accuracy. Nevertheless, they also highlighted the need for advanced GIS processing knowledge when developing a digital representation of the floodplain and channel terrain.

Paiva et al. (2011) demonstrated the use of SRTM DEM in a large-scale hydrologic model with a full 1-D hydrodynamic module to calculate flow propagation on a complex river network. The study was conducted on one of the major tributaries of the Amazon, the Purus River basin. They found that a model validation using discharge and water level data is capable of reproducing the main hydrological features of the Purus River basin. The authors concluded that it is possible to employ full hydrodynamic models within large-scale hydrological models even when using limited data for river geometry and floodplain characterization. This study continues the presented line of research and deals with the assessment of the effects of using different DEM data source (SRTM, ASTER and CARTODEM) in a 2-D hydraulic modelling of floods for a basin in North East India.

DEM products sometimes suffer from artefacts caused by data acquisition or processing. DEM smoothing is an important pre-processing step meant for removing these errors. Detailed description of DEM smoothing is discussed in the next section.

1.3 DEM smoothing

One of the biggest problems faced while analysing digital elevation models (DEM) produced using photogrammetry, is to avoid pits and peaks in DEM. The objective of smoothing algorithms is to remove certain high-frequency information in the DEM, while preserving genuine information at all frequencies. Smoothing algorithm preserves sharp features in the DEM, while removing noise. DEM smoothing algorithms are either linear or non-linear based methods.

Smoothing of images is often done with a low-pass filter, which reduces noise, but also blurs sharp features and details, such as edges. The majority of surface smoothing research has been in the context of surface fairing with the motivation of creating aesthetically pleasing surfaces using meshes. The classic Laplacian smoothing method Field (1988); Mencl and Muller (1999) is the fastest and simplest surface smoothing method. However, when applied to a noisy 3D surface, significant shape distortion and surface shrinkage result in addition to noise removal. To overcome the shrinkage problem, Taubin (1995) proposed a filtering method with positive and negative damping factors. A first-order filter with positive damping shrinks and smooths the mesh surface, while a first order filter with negative damping expands the surface, to compensate for shrinkage. This method is fast and simple, but still has the problem of distortion of prominent mesh features. In addition, if the parameters of the two filters are not chosen carefully, the algorithm can be numerically unstable. Desbrun et al. (1999) introduced diffusion and curvature flow into surface fairing and proposed a simple and numerically stable implicit filtering method, which can deal with irregular meshes. They overcome the problem of shrinkage by rescaling the mesh to preserve its volume. The algorithm however suffers from distortion of prominent mesh features. Kim and Rossignac (2005) developed a general autoregressive moving average filter approach. Through suitable choice of parameters, the filter can act as a low pass, high pass, band amplification or band attenuation filter, thus enabling it to filter out e.g. high frequency, noise and, at the same time, enhance or suppress certain features. However, it was found difficult to design a suitable filter that could preserve sharp, high frequency features at the same time as removing noise.

Surface fairing typically operates by minimizing a fairness or penalty function that favours smooth surfaces (Moreton and Sequin, 1992). One Methodology to smooth a surface consists of incrementally reducing its surface area. This can be accomplished by Mean Curvature Flow (MCF) which is a second order geometric flow. MCF can reduce noise, but also has some unsatisfactory side effects, including the creation of singularities and shrinkage. A great deal of research has focused on modified second-order flows that produce better results than MCF.

(Clarenz et al. 2000) proposed a modified MCF as an anisotropic diffusion of the surface. They determined threshold from a weighted sum of the principle curvatures to determine the surface locations where edge sharpening is needed. Tangential displacement is added to the standard MCF at these locations for sharpening the edges. Although, this algorithms produces results that tend to preserve sharp features, it is not a strict generalization of diffusion from images to surfaces. Another mesh-based modified MCF is proposed by (Ohtake et al. 2000) where a threshold on the mean curvature is used to stop over-smoothing. Anisotropic diffusion as a modified surface area minimization for height functions was proposed by (Desbrun el al. 1999). These level set and mesh based methods are all modifications of curvature flows and do not exhibit a sharpening of details.

DEM also suffer from striping artefacts which consists of successive ridges and troughs. This striping artefact is caused due to uncompensated mast motion error. The stripe artefacts rapidly propagate through subsequent analysis and significantly affect its usability for various applications. (Oimen, 2000) attempted to remove stripping artifacts from photogrammetric DEM by using spatial filters in spatial domain. These filters affect the true terrain, as well as the stripes, and therefore degrade the DEM's resolution. Fourier transform has demonstrated its potential for stripe removal (Arrell et al., 2008) as such artefact frequency components are easily identified in frequency domain rather than in its spatial counterpart. Unlike spatial filtering, filtering in the spectral domain can be applied to specific frequencies within a dataset, minimizing data smoothing and editing. Once these distinctive frequency components are identified they can be easily removed.

(Arrel et al., 2008) removed the artefact frequency by simple cut filter where the frequency component is replaced by zero. The problem with such method is that the identification and delineation of the error components is inherently subjective in those cases where the boundary between data and error is fuzzy and not crisp and should be performed only when the location of the anomalous frequencies within the Fourier spectrum data is clear. (Tarekegn and Sayama, 2013) proposed alternative method which removes the artefact frequency component by Gaussian Cut Filter (GCF) and a semi-automatic Adaptive Spectral Median filter (ASMF). They reported that GCF was effective in removing the stripes even though identification of the anomalous spectral component was done manually. The application of the method for larger window size is however constrained by computational memory requirement.

Sun et al. (2007) proposed a simple and fast smoothing algorithm, which removes noise effectively, while preserving mesh features such as sharp edges and corners. The method consists of two stages. First, the noisy face normals are filtered iteratively by weighted averaging of neighbouring face normal and then vertex positions are iteratively updated to agree with the denoised face normal in the second stage. The weight function used during normal filtering is much simpler than that used in previous algorithms making algorithm both fast and simple to implement.

Based on the advantages and disadvantages of several DEM smoothing algorithms, three algorithms i.e. low pass filter, enhanced lee filter and denoising algorithms based on Sun et al., (2007) were implemented in this study to remove noise from SRTM, ASTER and CARTODEM and to observe their effect on flood inundation simulations.

2. OBJECTIVES

IWRM is a process which promotes the coordinated development and management of water, land and related resources (Global Water Partnership, 2000). Keeping in view the importance of IWRM, National Institute of Hydrology (NIH), a premier Institute in the area of hydrology and water resources in India, set up regional centres for taking up studies relating to the field problems and also to develop closer interaction with the water resources organizations in different regions of the country. One such regional centre was set up at Guwahati for the North-Eastern Region catering for the various water resources problems of seven North East States, Sikkim and parts of West Bengal.

Considering flood as the major problem in the region, Ministry of Water Resources, Govt. of India decided to rededicate the Regional Centre towards service of the region and renamed it as NIH Centre for Flood Management Studies for the Brahmaputra Basin (NIH-CFMS).Under the mandate of XII plan period, the centre is working on a project in IWRM under Pilot Basin Study (PBS). The PBS program involves identification of suitable basin in consultation with concerned State Govt. authorities, establishment of advanced instrumentation for data collection and storage, data processing and analysis using state of the art models, preparation of results and findings in collaboration with specialists of other relevant disciplines in a meaningful and usable form for the intended beneficiaries and stake holders.

The Kulsi River Basin, a part of the Brahmaputra sub-basin, situated on the south bank of the mighty River Brahmaputra was identified for PBS study. The selected basin is ideal to develop flood inundation maps due to its strategic location encompassing two states in the north-east coupled with the fact that the region experiences maximum floods.

Most of the basins in North East India have insufficient hydrological gauge stations, which makes the reliance on availability of satellite products even more important for hydrologic simulations. The importance of topography has been highlighted in the previous section. Elevation data from different sources are widely available even for data-poor developing country. This study focuses their effect on floods simulations. DEM pre-processing plays an important role in final simulations and the impact of DEM smoothing on flood inundation mapping is considered in this study.

The objectives of the study are:

a) To generate flood inundation maps using RRI Model with different topographic data: SRTM, ASTER, and CARTODEM for Kulsi River Basin, and

b) To evaluate the impact of smoothing using low pass filter, enhanced lee filter, and denoising algorithms on flood inundation maps for Kulsi Basin.

3. STUDY AREA

3.1 Location

The Kulsi basin, a part of the Brahmaputra sub-basin, is situated on the south bank of the mighty river Brahmaputra (Fig 2.1). This sub-basin spreads in the Kamrup District of Assam as well as west Khasi hills and Ribhoi district of Meghalaya. It is located between latitude 25°30’N to 26°10’N and longitude 89°50’E to 91°50’E with an altitude between 100 m to 1900 m above msl. The total drainage area of Kulsi River is 2806 sq. km.

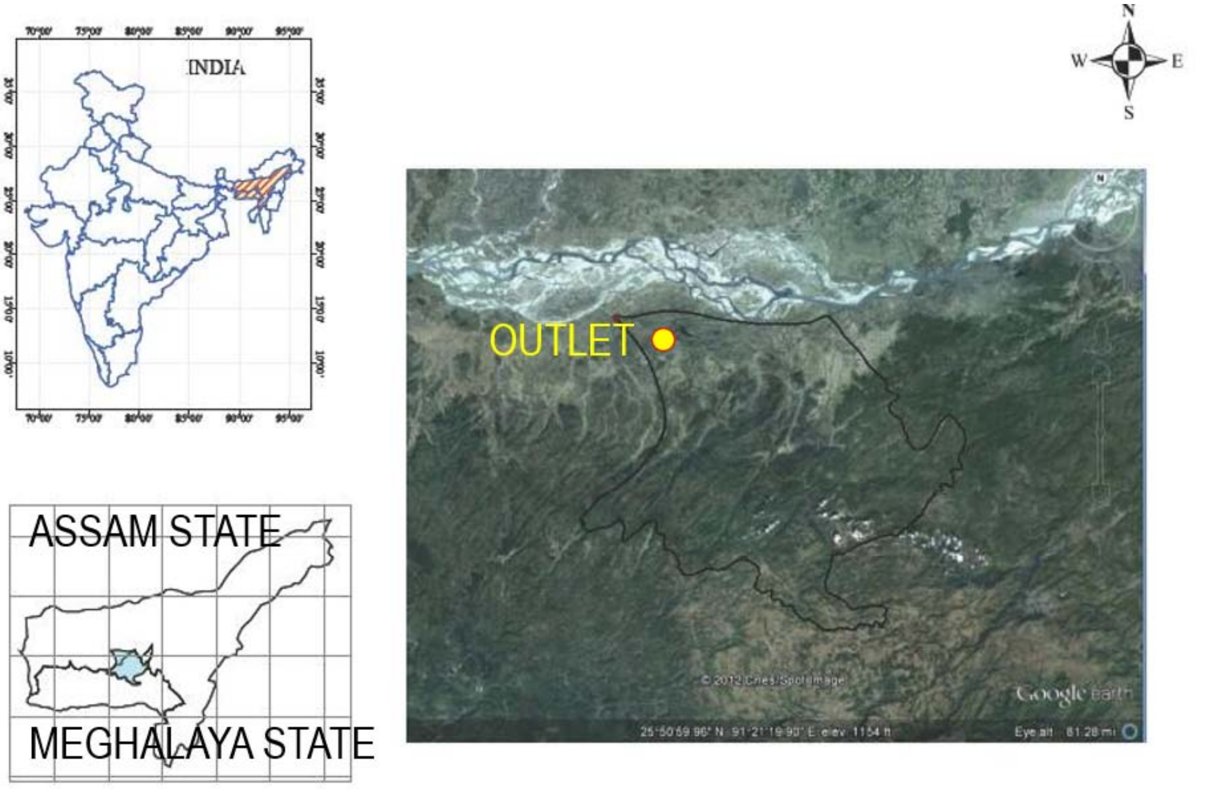

Fig 3.1 Location of Kulsi River Basin

3.2 River system

The Kulsi River is formed by the joining of three rivers namely Khari, Um Krishniya and Um Siri, all of which originate from the west Khasi Hills ranges and flows down north and joins the Brahmaputra (Fig 3.2). This hill range is covered with evergreen forests and gets high rainfall during the summer months. The river Um Krishniya is the centrally flowing river- with Um Siri joining it on the left bank and Um Khri joining it on the right bank. Um Krishniya and Um Siri originate almost from the same place, which is having the altitude around 1550m and Um Khiri originate from on area further east, which have got elevation around 1600m. All the three rivers are joined by innumerable number of small hilly streams and rivulets till they join together and flow down north by the name Kulsi.

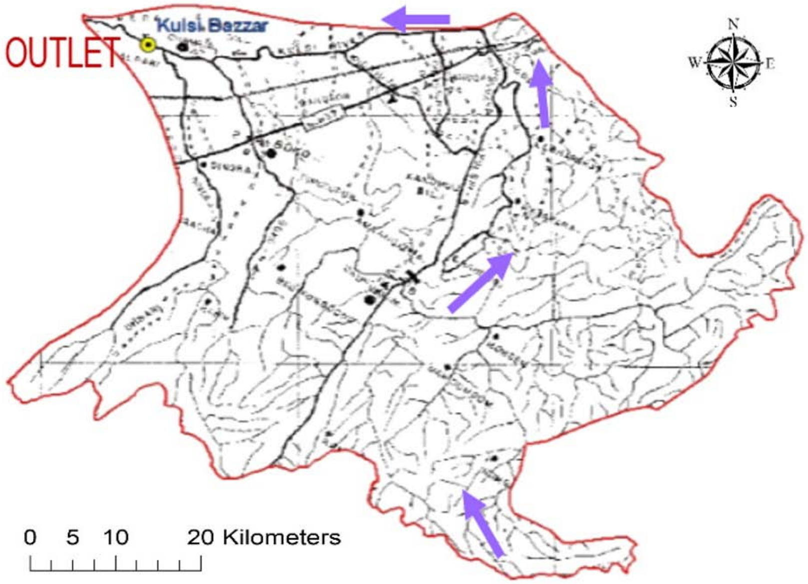

Fig 3.2River system of Kulsi River Basin

Source: Brahmaputra Board Master Plan, 2012

The river Khiri and Um Krishniya join together after they flow respectively for a distance of about 85 km. and 47 km. After joining, the river flows by the name Khri for a distance about 15 km. when it is joined by UmSiri, which flows for a distance of about 52 km. The central Kulsi again bifurcates into near village Hatigarh, and flows by the name Kharkhari and the other flows by the original name Kulsi. After these branches off, the river Kulsi enters into the alluvial plain (Flood plain of the river Kulsi and Brahmaputra) and gets shallow and meanders.

From village Kulsi, where the river Kulsi bifurcates, to its outfall at Brahmaputra near village Bahati, the river flows for a distance of about 100 km., making its total distance from source to outfall to be 220 km. out of which about 100km. is in Meghalaya and 120km. is in Assam. The drainage pattern of the Kulsi River systems is often found to be trellis and rectangular type in the upper catchment region, which developed due to structural control on the drainage network. The line diagram of Kulsi River system is shown in figure 3.3.

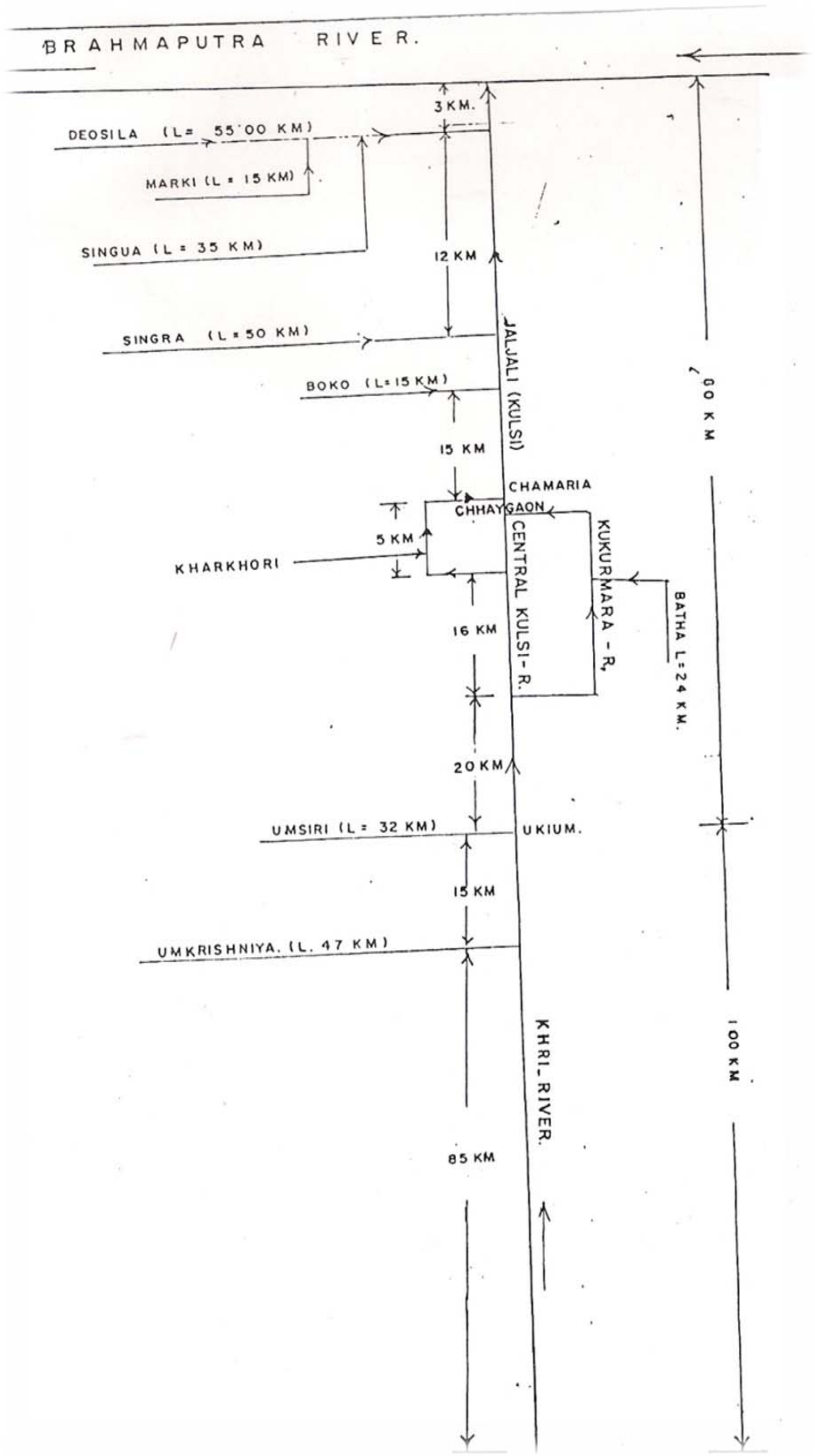

Fig 3.3 Line diagram of Kulsi River

Source: Brahmaputra Board Master Plan, 2012

3.3 Tributaries

The Kulsi River receives large number of tributaries in its various reaches. The Line Diagram of Kulsi River is shown in Figure 3.3. In the upper reach, it is joined by Krishniya and Umsiri on the left bank. In the middle reach its main tributary is Batha while in the flood plain reach it is joined by Boko and Singra. The catchment areas of the main tributaries of Kulsi are as follows (Table 3.1):

Table 3.1 Tributaries of Kulsi and their catchment area

Sl. No.	Name of the tributaries	Catchment area (Sq. Km)
1.	Krishniya	70 sq. km.
2.	Umsiri	295 sq. km.
3.	Batha	285 sq. km.
4.	Boko	250 sq. km.
5.	Singra	380 sq. km.

3.4 Climate

The climate of Kulsi basin, excluding the upper most reach is similar to that of the other districts in Central Assam. The winter is cold and foggy, while the summer is hot and humid. There is no meteorological centre within the catchment for observation of temperature. However the nearest observatories for the basin are at Guwahati, Umiam and Shillong. Based on long term data from these stations it has been observed that the average maximum temperature in this basin varies between 15^0C to 33^0C and average minimum temperature varies from 3^0C to 12^0C. The climate of this sub-basin is generally very humid. There is no meteorological Centre in the sub-basin for observation of humidity.

3.5 Geology

The geology of the river basin consists mostly of gneiss and sandstones overlain by a deep to moderately deep soil layer. Much of the terrain is rough, rolling to steeply sloping. Under saturated conditions, such a formation is highly conducive to rapid subsurface storm flow. The rock types in the Kulsi basin vary from Precambrian stage to recent. The surface Geological formation is newer alluvium sand, gravel, clay and silt. In Assam part of the basin falls in Kamrup District where two distinct groups of rock units i.e. consolidated and unconsolidated formation of rocks are found.

The Kulsi catchment is dominantly underlain by gneissic complex, Shillong group which have undergone regional metamorphism and later intruded by granite. The northern fringe of the hills is occupied by alluvial deposits of the Brahmaputra river system. The narrow valleys within the hills are filled up with coarse, angular grained grits and sand with silt & clay.

3.6 Landuse

The area that the Kulsi River drains can broadly be divided into three reaches

(i) The Upper Khasi hill reach

(ii) The middle reserve forest reach

(iii) The alluvial or flood plain reach

The Upper Khasi hill ranges of the catchment extend from the origin of the river Kulsi to Ukium (Assam Meghalaya border) and this reach lies entirely in the west khasi hill ranges, with the general altitude varying from 150 m to 1900 m. the whole area consists of series of hill range with intermittent plain areas. The upper reaches of the region is covered with evergreen and deciduous forest. However, most of the area represents degraded forest and in many places are covered by scrubs. No area in the reach remains under snow cover.

The middle reserve forest reach region consists of areas along the southern bank of river Brahmaputra. The region near Kulsi village, the river Kulsi branches off into three channels and all of them join together after flowing a distance of few kilometers downstream. The middle reserve forests reach consists of two reserve forests namely Borduar and Pantan reserve forest running parallel along the river from Ukium to Kulsi village with the Borduar reserve forest on eastern bank and Pantan reserve forest on the western bank. The river in this reach has got a very narrow valley running between these two reserve forests.

The alluvial or the plain reach consists of the plain areas along the southern bank of river Brahmaputra. Almost half of this reach is affected by the flood of the River Kulsi and the Brahmaputra. Just at the starting of this reach i.e. near village Kulsi, the river Kulsi branches off into three channels and all of them join together after flowing a few kms and outfalls into the Brahmaputra near Barak. This area is fully cultivable area and sufficiently densely populated.

The landuse consists primarily of evergreen forest, semi-evergreen forest, moist-deciduous forest, bamboo-thickets, jhum and rolling grasslands. The pattern of land use of the Kulsi basin area as follows:

1.	Degraded forest	62.33%
2.	Dense forest	15.56%
3.	Scrub	15.50%
4.	Jhum cultivation	0.50%
5.	Agricultural plantation	2.41%
6.	Agricultural land	2.37%
7.	Rivers	1.04%
8.	Water bodies	0.29%

Source: Brahmaputra Master Plan, 2012

3.7 Major flood events

Due to the drainage congestion for the flow of Kulsi River Basin, the region experiences frequent flood events. Normally the monsoon sets in over the study area during the first week of June and withdraws by the second week of October. The flooding events are concentrated during the summer monsoon months of June – September. Table 3.2 lists the extreme flood events witnessed in the study area in the last decade along with the damages incurred.

Table 3.2Flood damage trend in Kulsi River Basin

Year	**Average Annual Area (10^3 ha)**		**Flooded crop area % of total inundated area**	**Average number of people affected**	**Average damage Rs.(10^6)**
	Total	**Cropped**			
2001	0.87	0.18	20.68	86	0.586
2004	0.75	0.16	21.33	152	0.757
2007	1.01	0.30	29.71	200	1.518
2008	1.43	0.40	27.97	455	14.452
2010	1.07	0.38	35.51	586	31.717

Source: Brahmaputra Master Plan, 2012

The table lists the breakup of flooded crop area to the total area inundated by floods. In the period from 2000 – 2014 major flood events were experienced in years 2001, 2004, 2007, 2008 and 2010. The percentage of damaged cropped land and annual number of people is seen to be steadily increasing as the increasing population pressures forces people to live in the flood plains. The distribution of affected population as per Census report shows that 32.42 percent are workers, while 67.58 percent are non-workers. Cultivators comprised of 39.11%, agricultural workers 14.19 %, household industry workers 6.89 % and 39.81 % were other workers.

4. DATA ACQUISITION

4.1 Rainfall and discharge data

Daily rainfall data of twenty years from 1991 to 2011were collected from India Meteorological Department for five rain gauges in and around Kulsi River Basin. The distribution of the rain gauges is shown in figure 4.1. Out of the five rain gauges, the rain gauges located at Boko and Ukium fall within the basin, while rain gauges at Guwahati Airport, Dudhnoi and Mairang fall outside the River Basin. Daily discharge data is recorded at Kulsi Bazzar location which is at the outlet of the Kulsi River Basin. The daily discharge data from 1991 to 2011 was collected from Brahmaputra Board, Guwahati.

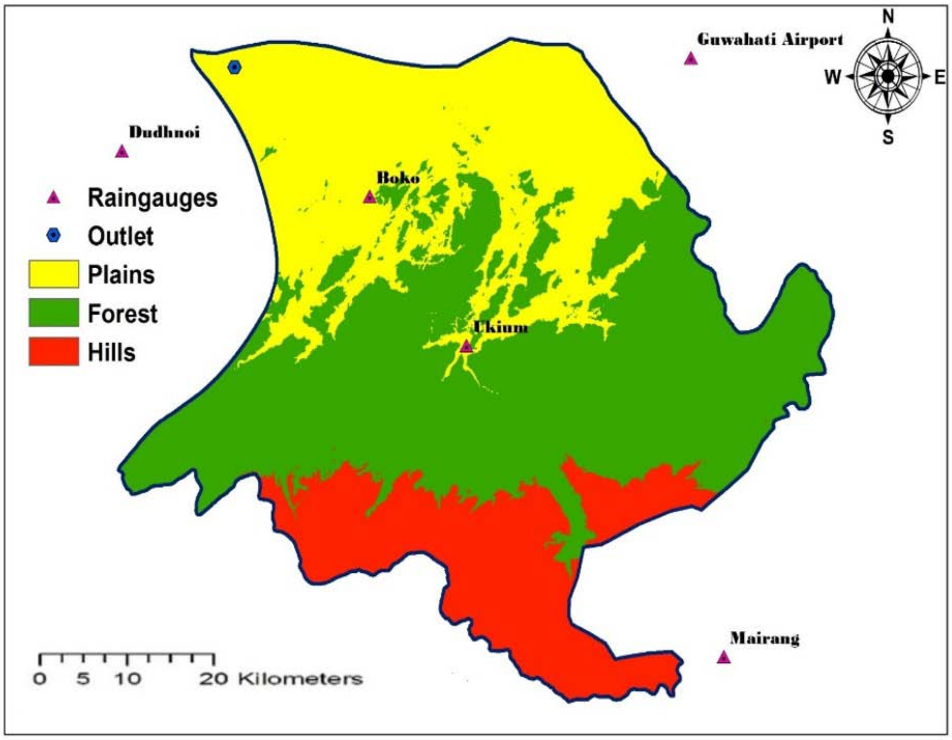

Fig 4.1Location of rain gauges and discharge Site

4.2 Topographic data

DEM were used in this study to characterize the topography of the study area. Hydrological data and maps based on SHuttle Elevation Derivatives at multiple Scales (HYDROSHEDS) constitute the high-resolution processed elevation data obtained during a Space Shuttle flight for NASA's Shuttle Radar Topography Mission (SRTM) at 90m resolution. The original SRTM data have been hydrologically conditioned using a sequence of automated procedures for developing HYDROSHEDS. The relevant topographic data were downloaded from (http://hydrosheds.cr.usgs.gov/dataavail.php).

Advanced Spaceborne Thermal Emission and Reflection Radiometer (ASTER) Global Digital Elevation Model (DEM) of 30 m resolution was also used in the study. The version 2 data consists of improved coverage and reduced artifacts. The data has been refined by production algorithm which provides improved spatial resolution, increased horizontal and vertical accuracy, and superior water body coverage and detection. The ASTER GDEM V2 maintains the GeoTIFF format and with 30-meter resolution. The data has been downloaded from the following site for the study (http://www.jspacesystems.or.jp/ersdac/GDEM/E/index.html).

CartoDEM is a National DEM developed by the Indian Space Research Organization (ISRO). It is derived from the Cartosat-1 stereo payload launched in May 2005. The methodology adopted to produce the CartoDEM involved stereo-strip triangulation of 500km strip stereo pairs using high precise ground control points, interactive cloud masking, and automatic dense conjugate pair generation using matching approach. The primary output unit is a tile of 7.5’ by 7.5’ extents with DEM spacing of 1/3 arc-sec. The data has been downloaded from (www.nrsc.gov.in). Table 4.1 shows the characteristics of different DEM used in the study.

Table 4.1 Characteristics of SRTM, ASTER and CARTO DEM

DEM source	SRTM	ASTER	CARTO
Satellite / Platform	Shuttle Radar Topography Mission	Advanced Spaceborne Thermal Emission and Reflection Radiometer	IRS-P5
Agency	NASA	NASA, METI, Japan	ISRO, India
Resolution	3 Arc Second (90m)	1 Arc Second (30m)	1 Arc Sec (30m)
Accuracy	16m	10 – 14 m	8 – 10 m
Launch	Feb 2000	Feb 2000	May 2005

4.3 Soil data

The soil data for the study has been obtained from the Harmonized World Soil Database v 1.2 of the FAO soil portal. The Harmonized World Soil Database is a 30 arc-second raster database with over 15 000 different soil mapping units that combines existing regional and national updates of soil information worldwide with the information contained within the 1:5 000 000 scale FAO-UNESCO Soil Map of the World . Over 16000 different soil mapping units are recognized in the Harmonized World Soil Database (HWSD) which are linked to harmonized attribute data. Use of a standardized structure allows linkage of the attribute data with GIS to display or query the composition in terms of soil units and the characterization of selected soil parameters

The soil data for the study area was downloaded from the FAO site with the URL as (http://www.fao.org/soils-portal/soil-survey/soil-maps-and-databases/harmonized-world-soil-database-v12). The soil texture of Kulsi River Basin consisted of sandy loam (29 %), sandy clay (25 %) and clay loam (46 %). The Phyisco-chemical properties of soil of Kulsi River Basin are given in table 4.2.

Table 4.2 Physico-chemical properties of soil

Soil Texture	Sandy Loam	Sandy Clay	Clay Loam
Rock fragment (%)	29.99	18.64	13.35
Sand (%)	49	48	36
Silt (%)	38	12	14
Clay (%)	13	40	50
Organic Carbon (%)	1.75	2.31	2.55
Bulk Density (gm/cm^3)	1.22	1.34	1.42
Available Water Content (mm water/mm soil)	0.1028	0.1027	0.1148
Hydraulic Conductivity (mm/hr)	1.69	1.54	1.36

5. MODEL DESCRIPTION

Rainfall-Runoff-Inundation (RRI) model has been used to model the hydrological behaviour of the Study Area. RRI is a two-dimensional model capable of simulating rainfall-runoff and flood inundation simultaneously (Sayama, 2012). The model deals with slopes and river channels separately. At a grid cell in which a river channel is located, the model assumes that both slope and river channel are positioned within the same grid cell. The channel is discretized as a single line along its centerline of the overlying slope grid cell. The flow on the slope grid cells is calculated with the 2D diffusive wave model, while the channel flow is calculated with the 1D diffusive wave models. For a better representation of rainfall-runoff-inundation processes, the RRI model also simulates lateral subsurface flow, vertical infiltration flow and surface flow.

The lateral subsurface flow, which is typically more important in mountainous regions, is treated in terms of the discharge-hydraulic gradient relationship, which takes into account both saturated subsurface and surface flows. On the other hand, the vertical infiltration flow is estimated by using the Green-Ampt model. The flow interaction between the river channel and slope is estimated based on different overflowing formulae, depending on water-level and levee-height conditions (Sayama, 2010). The model separates the grid cells as slope and river. The grid cell is assumed as both slope and river within the same grid cell for the location of river channel. RRI couples 1D diffusive wave model for channel flow and 2D diffusive wave model for slope. Figure 5.1 shows the schematic diagram of RRI model.

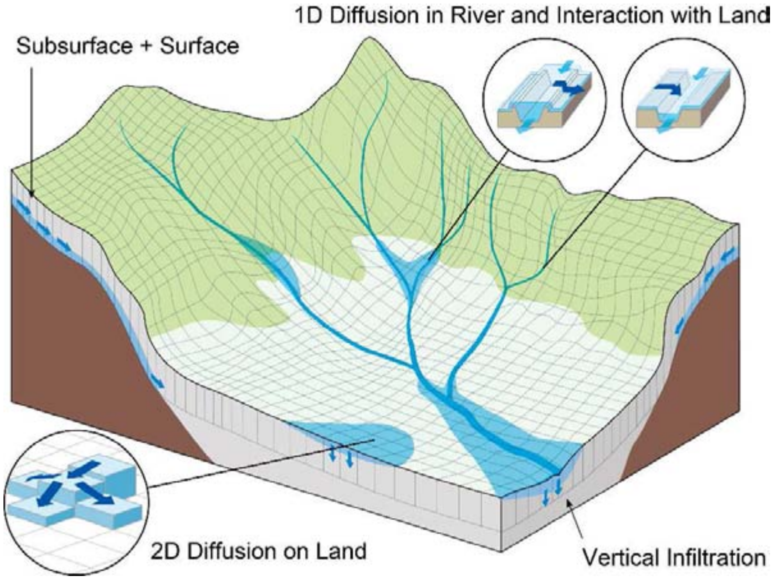

Fig 5.1 Schematic diagram of RRI model

Source: Sayama, 2010

5.1 Governing equations of RRI model

A method to calculate lateral flows on slope grid-cells is characterized as "a storage cell-based inundation model" (Hunter, 2007). The model equations are derived based on the following mass balance equation and momentum equation for gradually varied unsteady flow.

$$\frac{\partial h}{\partial t}+\frac{\partial q_x}{\partial x}+\frac{\partial q_y}{\partial y}=r-f \qquad (1)$$

$$\frac{\partial q_x}{\partial t}+\frac{\partial u q_x}{\partial x}+\frac{\partial v q_x}{\partial y}=-gh\frac{\partial H}{\partial x}-\frac{\tau_x}{\rho_w} \qquad (2)$$

$$\frac{\partial q_y}{\partial t}+\frac{\partial u q_y}{\partial x}+\frac{\partial v q_y}{\partial y}=-gh\frac{\partial H}{\partial y}-\frac{\tau_y}{\rho_w} \qquad (3)$$

h = height of the water from the local surface

q_x, q_y = unit width discharges in x and y directions

u, v = flow velocity in x and y directions

r = rainfall intensity

f = infiltration rate

H = height of the water from the datum

ρ_w = density of water

g = gravitational acceleration

τ_x, τ_y = shear stress in x and y directions

The second terms of the right side of (2) and (3) are calculated with the Manning's equation.

$$\frac{\tau_x}{\rho_w}=\frac{gn^2u\sqrt{u^2+v^2}}{h^{1/3}} \qquad (4)$$

$$\frac{\tau_y}{\rho_w}=\frac{gn^2v\sqrt{u^2+v^2}}{h^{1/3}} \qquad (5)$$

where, n is the Manning's roughness parameter.

Under the diffusion wave approximation, inertia terms are neglected in left side of equation (2) and (3) and the following equations are derived for x and y direction.

$$q_x=-\frac{1}{n}h^{5/3}\sqrt{\left|\frac{\partial H}{\partial x}\right|}\,sgn\left(\frac{\partial H}{\partial x}\right) \qquad (6)$$

$$q_y=-\frac{1}{n}h^{5/3}\sqrt{\left|\frac{\partial H}{\partial y}\right|}\,sgn\left(\frac{\partial H}{\partial y}\right) \qquad (7)$$

where sgn is the signum function.

The RRI model spatially discretizes mass balance equation (1) as follows:

$$\frac{dh^{i,j}}{dt} + \frac{q_x{}^{i,j-1} - q_x{}^{i,j}}{\Delta x} + \frac{q_y{}^{i,j-1} - q_y{}^{i,j}}{\Delta y} = r^{i,j} - f^{i,j} \tag{8}$$

Where $q_x{}^{i,j}, q_y{}^{i,j}$are x and y direction discharges from a grid cell at (i,j).

From the equation (6), (7) and (8), water depth and discharge can be calculated for each grid cell for each time step. RRI think about the different discharge hydraulic gradient relationship for surface flow and subsurface flow so it can simulate both condition flows with the same algorithm. RRI model use the following equations, which were originally conceptualized by Ishihara and Takasao (1962) and formulated with a single variable by Takasao and Shiiba (1976, 1988) based on kinematic wave approximations.

Equation (9) and (11) describe the saturated subsurface flow and the equation (10) and (12) describe the combination of the saturated subsurface flow and surface flow based on the Darcy law. For the kinematic wave model, hydraulic gradient is assumed to the topographic slope and RRI model assumes the water surface slope as the hydraulic gradient.

$$q_x = -k_a h \frac{\partial H}{\partial x} (h \leq d) \tag{9}$$

$$q_x = -\frac{1}{n}(h - d_a)^{5/3} \sqrt{\left|\frac{\partial H}{\partial x}\right|} sgn\left(\frac{\partial H}{\partial x}\right) - k_a(h - d_a)\frac{\partial H}{\partial x} (d_a < h) \tag{10}$$

$$q_y = -k_a h \frac{\partial H}{\partial y} (h \leq d) \tag{11}$$

$$q_y = -\frac{1}{n}(h - d_a)^{5/3} \sqrt{\left|\frac{\partial H}{\partial y}\right|} sgn\left(\frac{\partial H}{\partial y}\right) - k_a(h - d_a)\frac{\partial H}{\partial y} (d_a < h) \tag{12}$$

where k_a is the lateral saturated hydraulic conductivity and d_a is the soil depth times the effective porosity.

The following equation (13) can be also used to simulate the effect of unsaturated, saturated subsurface flow and surface flow with the single variable of h (Tachikawa, 2004) (Sayama M. , 2009).

$$q_x = \begin{cases} -k_m d_m \left(\frac{h}{d_m}\right)^{\beta} \frac{\partial H}{\partial x}, & (h \leq d_m) \\ -k_a(h - d_m)\frac{\partial H}{\partial x} - k_m d_m \frac{\partial H}{\partial x}, & (d_m < h \leq d_a) \\ -\frac{1}{n}(h - d_a)^{5/3} \sqrt{\left|\frac{\partial H}{\partial x}\right|} sgn\left(\frac{\partial H}{\partial x}\right) - k_a(h - d_m)\frac{\partial H}{\partial x} - k_m d_m \frac{\partial H}{\partial x}, & (d_a < h) \end{cases} \tag{13}$$

5.2 Calculation of channel geometry

In RRI model, one dimensional diffusive wave model is used for river channel and the geometry is assumed as rectangle when detail river cross section is not available. The river width and depth are approximated by using the following functions according to the upstream contributing area in square kilometre.

$W = C_w A^{s_w}$

$D = C_D A^{s_D}$

Where,

$W = widthinmeter$

$D = depthinmeter$

$A = Areainsquarekilometer$

$C_w, S_w = widthparameters$

$C_d, S_d = depthparameters$

5.3 Interaction between slope and river cells

Water exchange between a slope grid cell and river grid cell is calculated at each time step depending on the relationship among the levels of slope water, river water, levee height and ground. The figure below shows four different conditions and for each condition, different overtopping formulae are applied to calculate the unit length discharge from slope to river (q_{sr}) or from river to slope (q_{rs}), which are then multiplied by the length of the river vector at each grid cell to calculate the total exchange flow rate. (Iwasa, 1982)

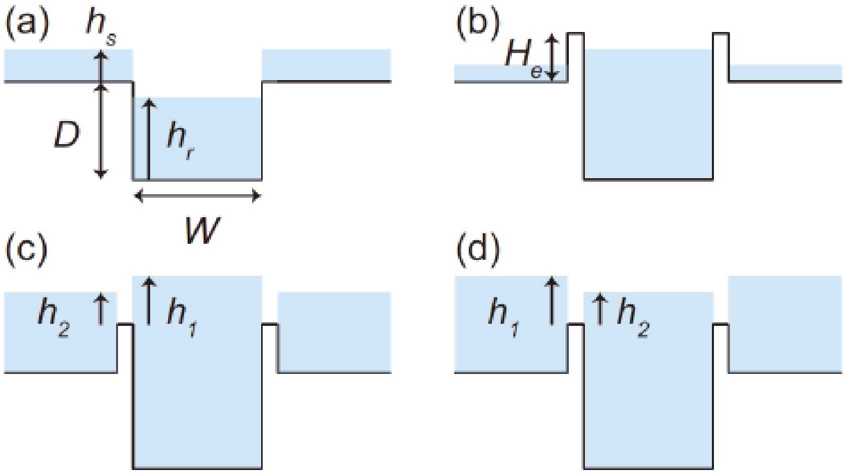

Fig 5.2 River and slope water exchange

(Sayama T. , Rainfall-Runoff-Inundation (RRI) Model, User's Manual)

When water level in the river cell is lower than the ground level, water from the slope cell will flow to the river and the following formula is used for calculation of discharge per unit width.

$$q_{sr} = \mu_1 h_s \sqrt{g h_s}$$

Where,

μ_1= constant coefficient

h_s= water depth on slope cell

5.4 Runge-Kutta Method

The Runge-Kutta methods are an important family of iterative methods for the approximation of solution of ordinary differential equations. RRI model use the fifth order Runge-Kutta method with adaptive time step control. This method solve an ordinary differential equation by the general fifth order Runge-Kutta formula and estimate its error by an embedded fourth order formula to control the time step. (Cash. J.R, 1990).The general form of fifth order Runge-Kuttha formula is

$$k_1 = \Delta t f(t, h_1)$$

$$k_2 = \Delta t f(t + a_2 \Delta t, h_1 + b_{21} k_1)$$

$$k_3 = \Delta t f(t + a_3 \Delta t, h_1 + b_{31} k_1 + b_{32} k_2)$$

$$k_4 = \Delta t f(t + a_4 \Delta t, h_1 + b_{41} k_1 + b_{42} k_2 + b_{43} k_3)$$

$$k_5 = \Delta t f(t + a_5 \Delta t, h_1 + b_{51} k_1 + b_{52} k_2 + b_{53} k_3 + b_{54} k_4)$$

$$k_5 = \Delta t f(t + a_6 \Delta t, h_1 + b_{61} k_1 + b_{62} k_2 + b_{63} k_3 + b_{64} k_4 + b_{65} k_5)$$

$$h_{t+1} = h_t + c_1 k_1 + c_2 k_2 + c_3 k_3 + c_4 k_4 + c_5 k_5 + c_6 k_6 + O(\Delta t^6)$$

While the embedded forth order formula (Cash. J.R, 1990) is

$$h^*{}_{t+1} = h_t + c^*{}_1 k_1 + c^*{}_2 k_2 + c^*{}_3 k_3 + c^*{}_4 k_4 + c^*{}_5 k_5 + c^*{}_6 k_6 + O(\Delta t^5)$$

By subtracting $h^*{}_{t+1} - h_{t+1}$,the error can be estimated by using $k_1 to k_6$ as follows,

$$\delta \equiv h_{i+1} - h^*{}_t \equiv \sum_{i=1}^{6} (c_i - c^*{}_i) k_i$$

5.5 Infiltration

Infiltration is the process of water entry into a soil from rainfall, snowmelt, or irrigation. Soil water movement is the process of water flow from one point to another within soil. Rate of infiltration is controlled by the rate of soil water movement below the surface and the soil water movement continues after the infiltration event, as infiltrated water is redistributed. The soil properties affecting soil water movement are hydraulic conductivity and water retention characteristic. Hydraulic conductivity is a measure of the ability of the soil to transmit water and depends upon both the properties of soil and the water. Total porosity, pore size distribution, and pore continuity are the important factors affecting hydraulic conductivity. The hydraulic conductivity at or above the saturation point is referred to saturated hydraulic conductivity, and for water content below saturation is called the unsaturated hydraulic conductivity. The water retention characteristic of the soil describes the soil's ability to store and release water and is defined as the relationship between the soil water content and the soil suction or metric potential.

5.6 Green-Ampt model

The Green-Ampt infiltration model is a simplified physical model and based on the Richard equation. It related the rate of infiltration to measurable soil properties such as the porosity, hydraulic conductivity, and moisture content of a particular soil. The advantages of Green-Ampt infiltration equation to Richard equation are that the analytical solution available for the computation of wetting front location and only two parameters of soil properties are required. The equation for Green-Ampt infiltration model to calculate infiltration losses is as follow.

$$f = k_v\left[1 + \frac{(\emptyset - \theta_i)S_f}{F}\right]$$

$k_v = verticalsaturatedhydraulicconductivity$

$\emptyset = soilporosity$

$\theta_i = initialwatercontent$

$S_f = suctionattheverticalwettingfront$

$F = cumulativeinfiltrationdepth$

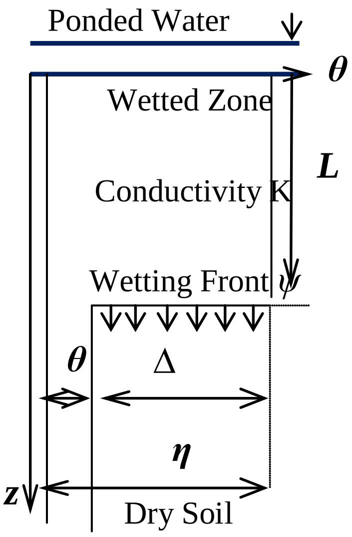

Fig 5.3 Schematic representation of Green and Ampt infiltration model

Source: V. T. Chow 1964

6. METHODOLOGY

The flowchart of methodology adopted in this study is shown in figure 6.1.

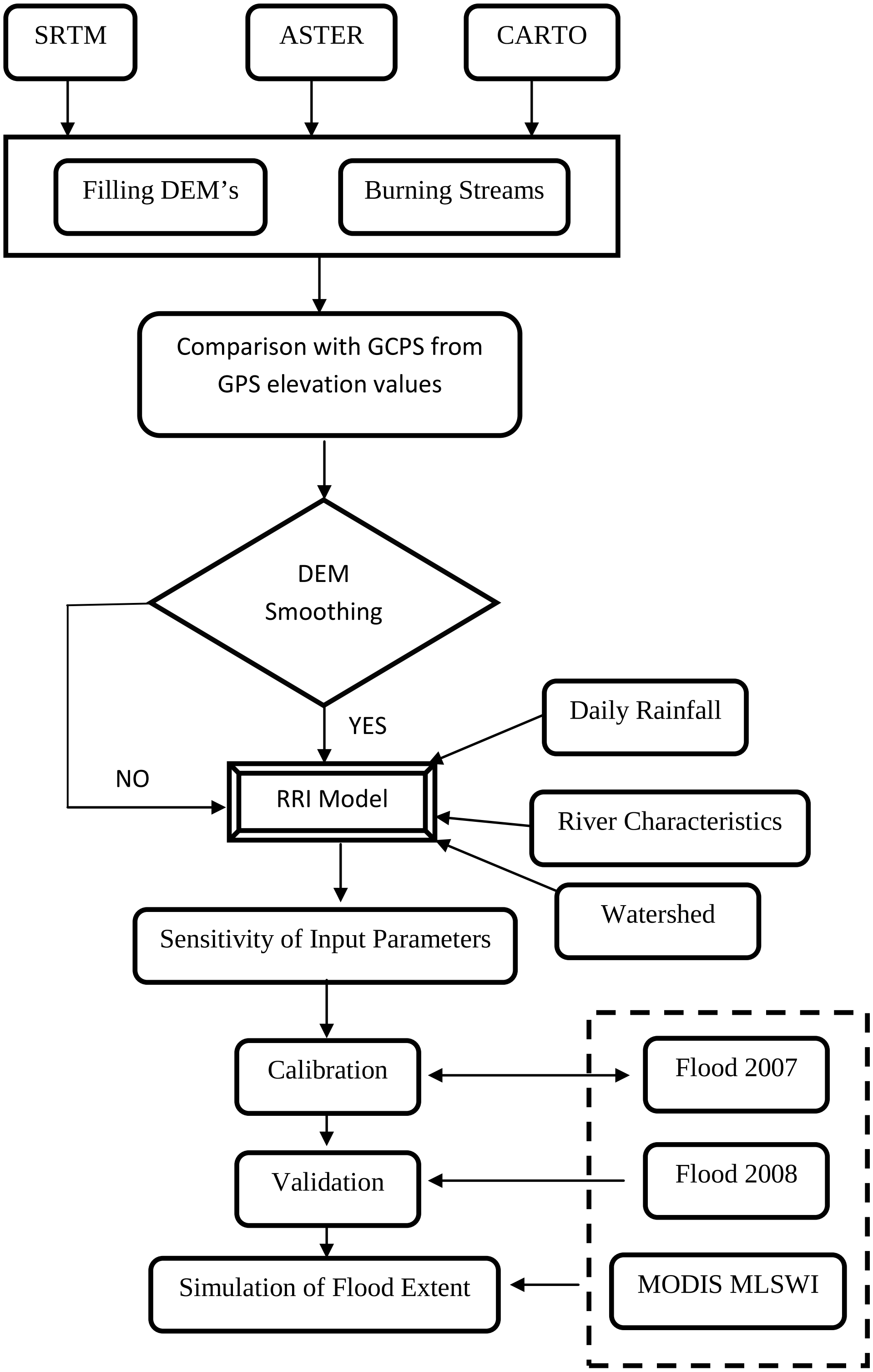

Fig 6.1Flowchart of methodology

6.1 Method description

The topographic data consisting of SRTM, ASTER and CARTO DEM were processed using ArcGIS Software. The accuracy of DEM was compared with elevation values of Ground Control Points (GCPs) obtained from Differential Geographic Positioning System (DGPS). DEM smoothing was carried out using low pass filter, enhanced lee filter (window size = 3), enhanced lee filter (window size =5) and denoising algorithm. Flow direction and flow accumulation were computed from the processed DEM. Elevation, flow direction and flow accumulation grids were exported into ASCII format to be used as input in RRI model.

Rainfall – Runoff data corresponding to the flood event observed in the study area for the year 2007 were selected for calibrating the RRI model. RRI model was set up to simulate the flow of Kulsi River at Kulsi Bazzar. Calibration of RRI model was carried out by matching the simulated hydrograph with observed hydrograph for the year 2007. Scenarios of sensitivity check were performed with RRI input parameters in order to study their influence on hydrologic simulations. Validation of RRI model was performed by executing the RRI model with the calibrated parameters for the year 2008.

Remote sensing images from Moderate Imaging Spectroradiometer (MODIS) were used to determine the flood inundation extent in Kulsi River Basin. Modified Land Surface Water Index (MLSWI) was used to identify the flooded areas. MLSWI was calculated using equation 6.1 as:

$$\text{MLSWI} = \frac{1-R_{NIR}-R_{SWIR}}{1-R_{NIR}+R_{SWIR}} \tag{6.1}$$

Where, NIR: near infrared reflectance; SWIR: short wave infrared reflectance. R_{NIR} and R_{SWIR} are reflectance values (R) of MODIS bands 2 and 6 or 7, respectively. An optimal threshold of MLSWI was selected as 0.64 to separate water bodies from other land-cover features based on the spectral characteristics (Kwak et al, 2013).The flood extent determined from MLSWI were used to access the accuracy of RRI model simulations based on different DEM, with and without smoothing.

6.2 Preparation of rainfall data

In this study gauged rainfall data from five stations spread in and around Kulsi River basin were used as input. The daily rainfall data corresponding to the monsoon months of June, July, August, September and October for the year 2007 was selected as input in the RRI model. Thiessen polygon method of interpolation was used for interpolating rainfall data for the RRI simulation. Figure 6.2 shows the rainfall distribution using the thiessen polygon interpolation in the Kulsi River basin for the year 2007.

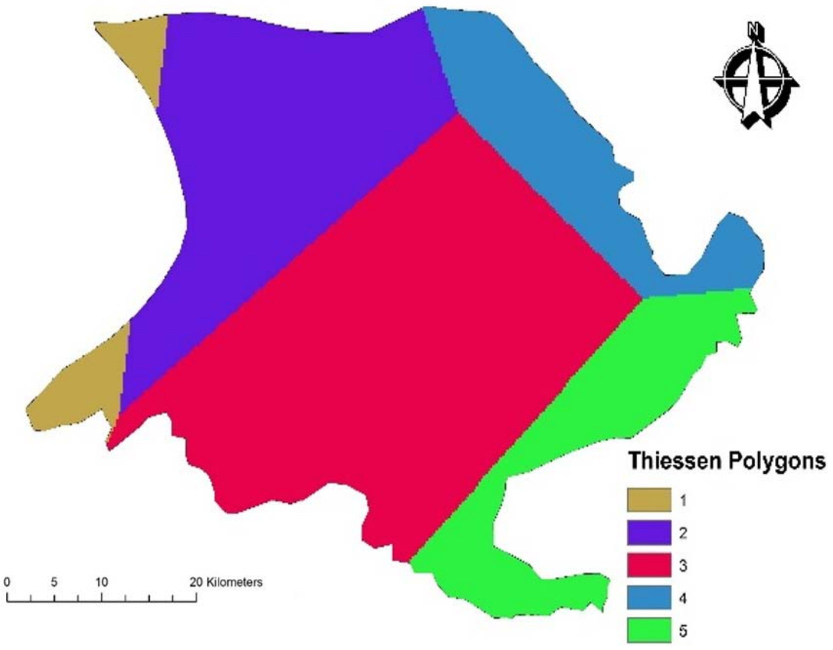

Fig 6.2 Distribution of rainfall using Thiessenpolygons

6.3 Preparation of soil data

The soil data for the study has extracted taken from the Harmonized World Soil Database v 1.2 of the FAO soil portal. The raster data was converted into ASCII format as input into RRI model. Figure 6.3 shows the distribution of soil in Kulsi River Basin. The figure shows distribution of clay loam type of soil in the plain areas, sandy clay soil in forest area and sandy loam in the hilly areas.

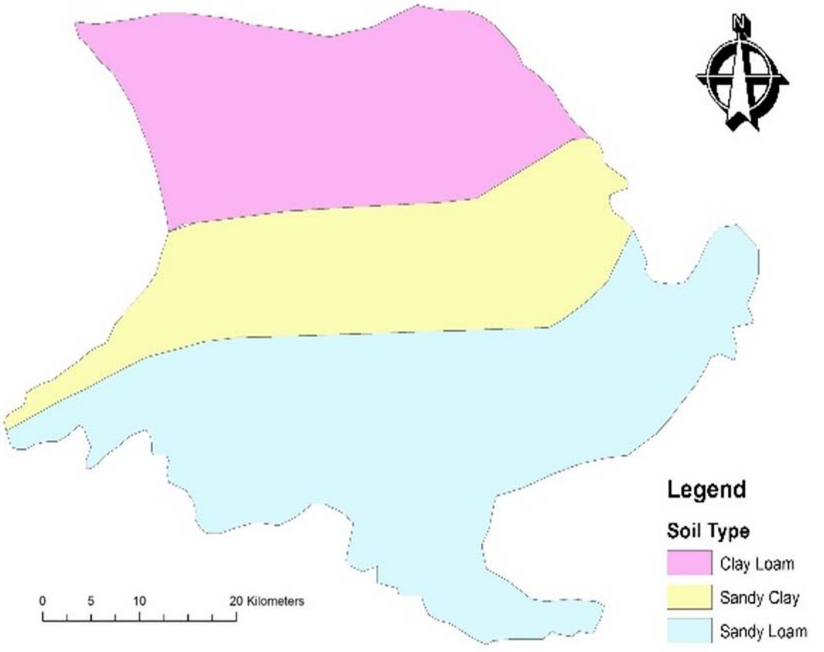

Fig 6.3Distribution of soil type in Kulsi River Basin

6. 4 Generation of Ground Control Points (GCP)

Elevation values were measured at fifty locations along the Kulsi River using Global Positioning System (GPS). The measurements were part of water quality experiment conducted by NIH in 2012. Out of fifty, twenty measurements were taken in flood plain and the remaining thirty in the forest and hill area. The GPS measurements constituted the Ground Control Points (GCP) for the study in order to compare the accuracies of different DEM.

6.5 Calibration of RRI model

RRI model was calibrated by adjusting the Manning's roughness of the basin and that of the river bed, depth of the soil and infiltration parameters. The manning's roughness used was derived from soil texture properties. Soil depth in water bodies was considered to be zero (0) since it is already saturated. Soil infiltration was estimated using the Green-Ampt Model based on the soil distribution of Kulsi River Basin. The Green-Ampt infiltration parameters are as shown in Table 6.2.

Table 6.2 Green-Ampt infiltration parameters

Texture	Porosity	Suction Head, (m)	K_{sv} (m/s)
Sand	0.437	0.0495	6.54E-05
Loamy Sand	0.437	0.0613	1.66E-0.5
Sandy Loam	0.453	0.1101	6.06E-06
Loam	0.463	0.0889	3.67E-06
Silt Loam	0.501	0.1668	1.89E-06
Sandy Clay Loam	0.398	0.2185	5.56E-07
Clay Loam	0.464	0.2088	5.56E-07
Silty clay loam	0.471	0.2730	5.56E-07
Sandy Clay	0.430	0.2390	3.33E-07
Silty Clay	0.470	0.2922	2.78E-07
Clay	0.475	0.3163	1.67E-07

Source; Handbook of Hydrology (Maidment, 1993)

The calibrated RRI model performance was quantified using three indices i.e. coefficient of correlation (r^2), Nash Sutcliffe Model Efficiency (NSE) and Root Mean Square Error (RMSE). Coefficient of correlation (r^2) is normally used to quantify the linear correlation between two sets of data. The range of r^2 lies between minus one (-1) and one (1); a value of r^2 = 0 means that there is no linear correlation at all between the two sets of data (observed data and simulated data) while a value of r^2> 0.5

are considered acceptable (Moriasi et al., 2007). The formula for correlation coefficient is given equation (15) as :

$$r^2 = \frac{\sum_{i=1}^{n}(x_i - \overline{x}) \cdot (y_i - \overline{y})}{\sqrt{\sum_{i=1}^{n}(x_i - \overline{x})^2 \cdot \sum_{i=1}^{n}(y_i - \overline{y})^2}} \tag{15}$$

Where n is the frequency of observation, *x* and *y* refer to the measured data

Nash-Sutcliffe Coefficient of Efficiency (NSCE)is a normalized statistic that determines the relative magnitude of errors compared to the variance of observed data. NSCE indicates how well the plot of observed data versus simulated data fits on the 1:1 line. NSCE = 1 indicate perfect match of simulations and observed data while values below zero indicate that the model does not represent physical conditions. NSCE is given by equation (16) as:

$$NSCE = \frac{\sum\left(Q_{i,o} - Q_{i,c}\right)^2}{\sum\left(Q_{i,o} - \overline{Q_o}\right)^2} \tag{16}$$

Where $Q_{i,c}$simulated discharge at the ith step,$Q_{i,o}$ is the observed discharge at the ith step and Q_o is the average discharge.

Nash-Sutcliffe efficiencies can range from -∞ to 1. An efficiency of 1 (E = 1) corresponds to a perfect match between model and observations. An efficiency of 0 indicates that the model predictions are as accurate as the mean of the observed data, whereas an efficiency less than zero ($-\infty < E < 0$) occurs when the observed mean is a better predictor than the model. Essentially, the closer the model efficiency is to 1, the greater is the accuracy of the model.

Root Mean Square Error (RMSE) is a frequently used measure of the difference between values predicted by a model and the values actually observed from the environment that is being modelled. These individual differences are also called residuals, and the RMSE serves to aggregate them into a single measure of predictive power. The RMSE of a model prediction with respect to the estimated variable X_{model} is defined as the square root of the mean squared error:

$$RMSE = \sqrt{\frac{\sum_{i=1}^{n}(X_{obs,i} - X_{model,i})^2}{n}} \tag{17}$$

Where, X_{obs} is observed values and X_{model} is modelled values at time/place *i*.

To verify the correspondence between flooded areas by RRI and flooded area by MODIS, Critical Success Index (CSI) categorical verification statistics was used. The CSI is computed using the following formula:

$$\text{CSI} = \frac{\text{RRI(area)} \cap \text{MODIS (area)}}{\text{RRI (area)} \cup \text{MODIS (area)}} \tag{18}$$

7. RESULTS

7.1 Topographic data processing

The DEM obtained online usually consist of errors classified as sinks or peaks. A sink is an area surrounded by higher elevation values, while a peak is defined as an area surrounded by lower elevation values. To create an accurate representation of flow direction and, therefore, accumulated flow, it is best to use a DEM that is free of sinks. A digital elevation model (DEM) that has been processed to remove all sinks and peaks is called a depressionless DEM. The depressionless DEM were created in the study using the *fill sink* tool available in ArcGIS software. Flow direction (DIR) and flow accumulation (ACC) for the DEM were also computed using Spatial Analyst Extension in ArcGIS. A subroutine available in RRI model *DemAdjust2.exe* was executed to further correct the values of flow direction and accumulation by employing the cut and fill operations of elevations.

Coarse resolution DEM are not able to replicate flow patterns especially in flat terrains. Hence, stream burning was carried out for all the DEM, which consists of lowering the relative positions of stream pixels by uniform depth. In order to carry out stream burning, the flow path of Kulsi River was digitized using information from Google Earth. Figure 7.1 shows the digitized stream network of Kulsi River. The digitized river network was burned into DEM using algorithm available in *ArcHydro* Tool.

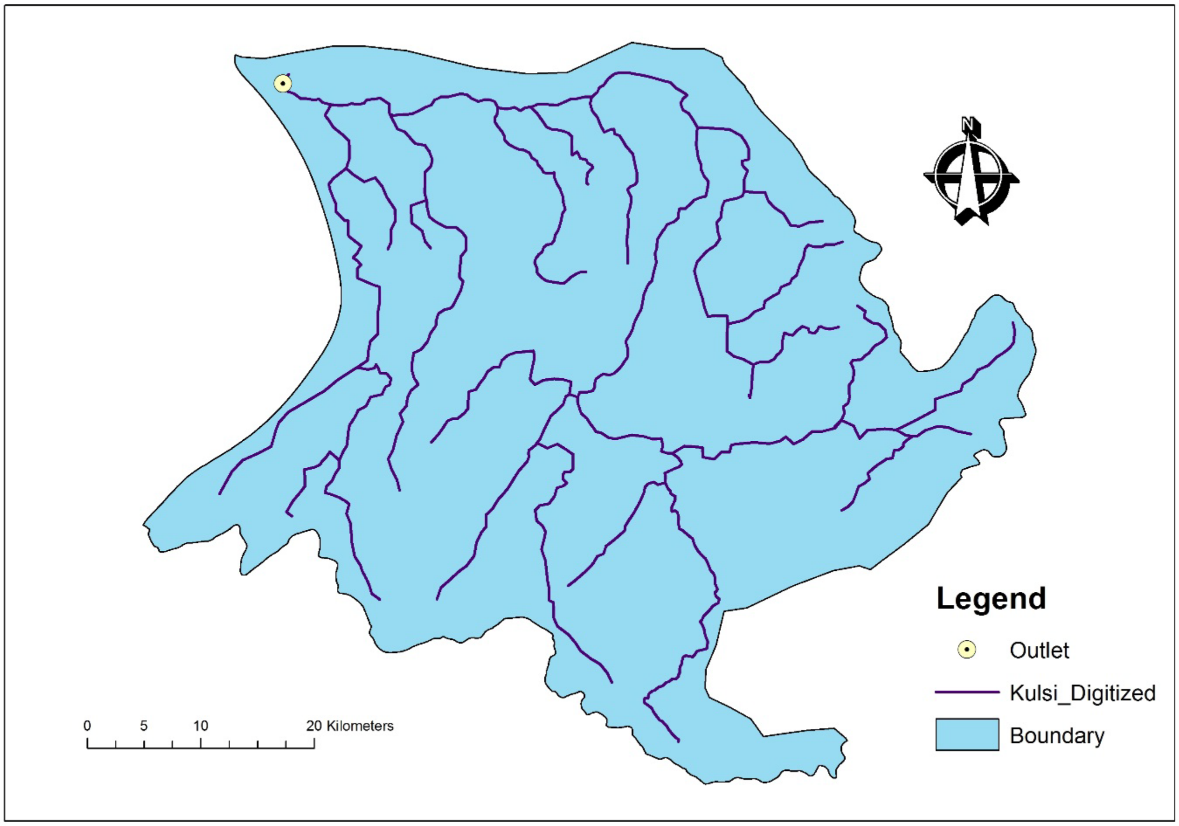

Fig 7.1 Digitized stream network of Kulsi River

The processed SRTM, ASTER and CARTO DEM were obtained as shown in Fig 7.2. On visual inspection, all the DEM exhibited similar trends in spatial distribution of specified elevation ranges, with exception of lowest and highest elevation values.

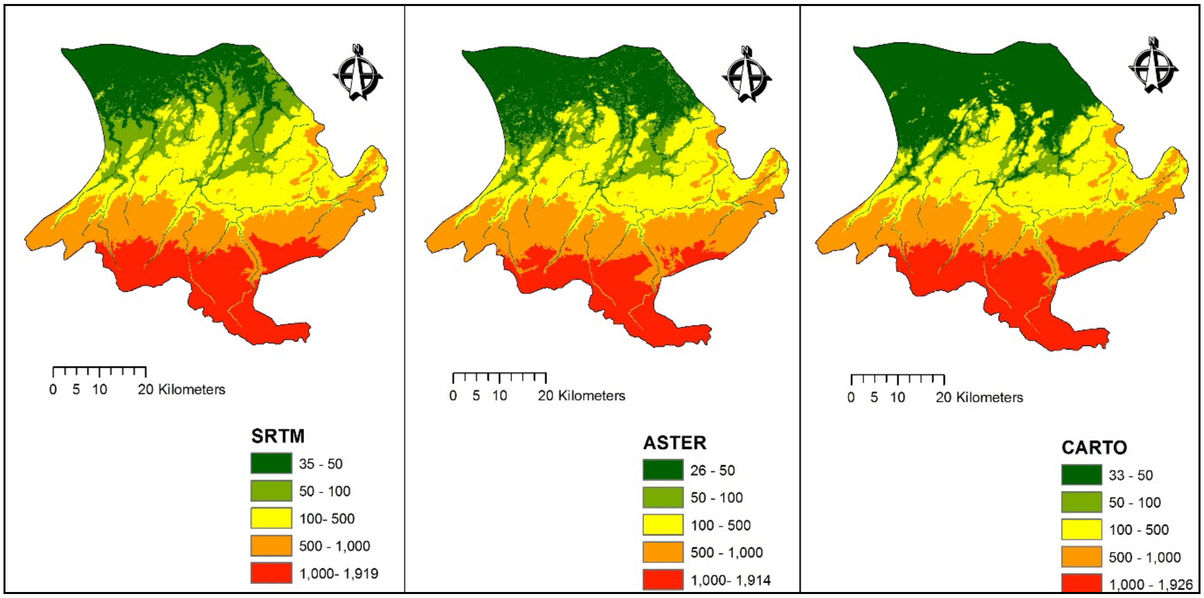

Fig 7.2 Processed DEM used in the study

Table 7.1 shows the basic statistics derived from the processed DEM. Highest elevation value was observed for CARTO DEM followed by SRTM and ASTER DEM respectively. The highest mean elevation and standard deviation was observed for SRTM DEM.

Table 7.1Basic statistics of processed DEM

Basic Statistics	SRTM	ASTER	CARTO
Minimum elevation (m)	35	26	33
Maximum elevation (m)	1919	1914	1926
Mean elevation (m)	869.1	833.5	852.7
Standard deviation	539.6	551.6	541.3

In order to determine the accuracy of DEM, fifty ground based elevations, represented by GPS measurements were compared with SRTM, ASTER and CARTO DEM's. The value of GPS measurements were converted into point shapefile. The point shapefile was defined with geographic projection system corresponding to the projection system of the DEM. The grid values corresponding to the location of individual point locations were extracted using Grid to Point tool in ArcGIS. The GPS measurements were classified into two categories, one consisting of GPS values located in flood plains and the other consisting of GPS values located in the forest and hilly area. Fig 7.3 shows the differences in elevation values observed for the flood plains from different DEM sources when compared with GPS elevations.

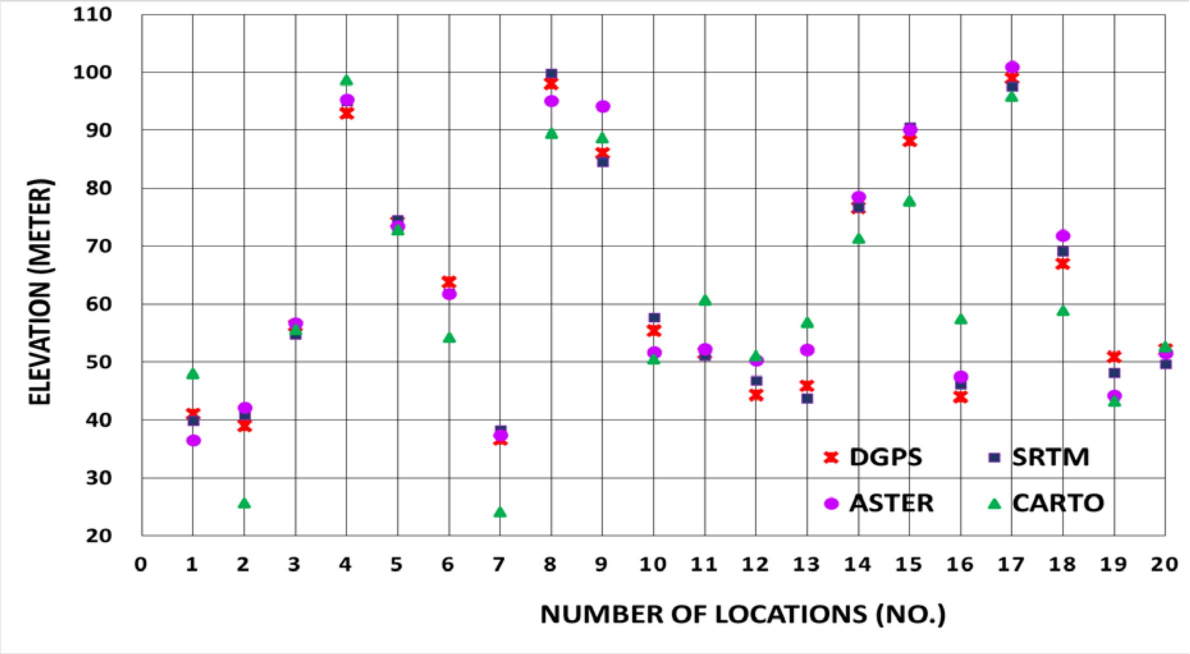

Fig 7.3 Comparison of elevation of GPS points with elevation of SRTM, ASTER and CARTO DEM for flood plain

In order to quantify the differences in elevation between the elevation of GPS points and DEM data RMSE and MAE values were computed separated for flood plain region and for the rest of the study area as shown in Table 7.2.

Table 7.2Comparison of SRTM, ASTER and CARTO DEM with elevation of GPS

Source of DEM	Flood Plain		Forest and Hills	
	RMSE (m)	MAE (m)	RMSE (m)	MAE (m)
SRTM	1.88	1.73	9.53	8.82
ASTER	3.85	3.15	6.95	5.94
CARTO	8.08	7.08	8.81	10.46

Based on the computed error analysis it can be observed that SRTM DEM produces the least RMSE and MAE for the flood plains i.e. 1.88 m and 1.73 m respectively, however for the remaining study area the best results for RMSE and MAE are obtained for ASTER DEM i.e. 6.95 m and 5.94 m respectively.

The performance of SRTM DEM for flood plains can be attributed to spatial resolution of SRTM DEM 90m which averages the elevation values for 90m by 90 m area, while for ASTER and CARTO DEM the average area is only 30 m by 30m. The minor elevation differences get averaged out for SRTM DEM resulting in lowest RMSE and MAE values. The lower resolution of SRTM however fails to capture the changes in actual elevation values in the hilly and forest areas compared with ASTER and CARTO DEM which exhibit better RMSE and MAE values for the same.

Pixel to pixel comparison of DEM was also carried out for the flood plain in order to quantify the difference among the elevation dat. In order to carry out the comparison the SRTM DEM were resampled to 30 m resolution corresponding to ASTER and CARTO DEM. Figure 7.4 shows the difference between SRTM and ASTER, ASTER and CARTO DEM and SRTM and CARTO DEM respectively.Spatial distribution of differences in elevation values among DEM showed that for forest and hill areas, SRTM DEM shows relatively high variation compared to CARTO and ASTER DEM. The percentage of pixels with elevation difference higher than 12 m were relatively higher when comparing SRTM with ASTER and CARTO DEM. Comparison of ASTER and CARTO DEM shows that majority of the elevation difference are within -4.0 m to 4.0 m range.

Table 7.3 shows the percentage of pixels falling within the flood plains for which elevation values underestimated, same and overestimated among the DEM. Based on Table 4.2 it can be observed that most of the difference between the DEM sources occur between – 6.0 m to + 8.0 m range. This range is within the range of error values reported for the DEM.

Table 7.3Pixel to pixel comparison of SRTM, ASTER and CARTO DEM

Elevation Difference (ED) (m)	**Flood Plain (% area)**		
	SRTM-ASTER	**ASTER-CARTO**	**SRTM-CARTO**
-6.0< ED < 0 m (under estimation)	24	29	30
(same elevation)	05	17	04
0 < ED < 8 m (over estimation)	71	54	66

The elevation values of SRTM DEM are found to be generally higher than ASTER DEM followed that by CARTO DEM. ASTER and CARTO DEM are closer in terms of elevation differences compared to SRTM DEM. The original resolution of 30 m for both CARTO and ASTER DEM could be attributed for observing least difference among CARTO and ASTER DEM.

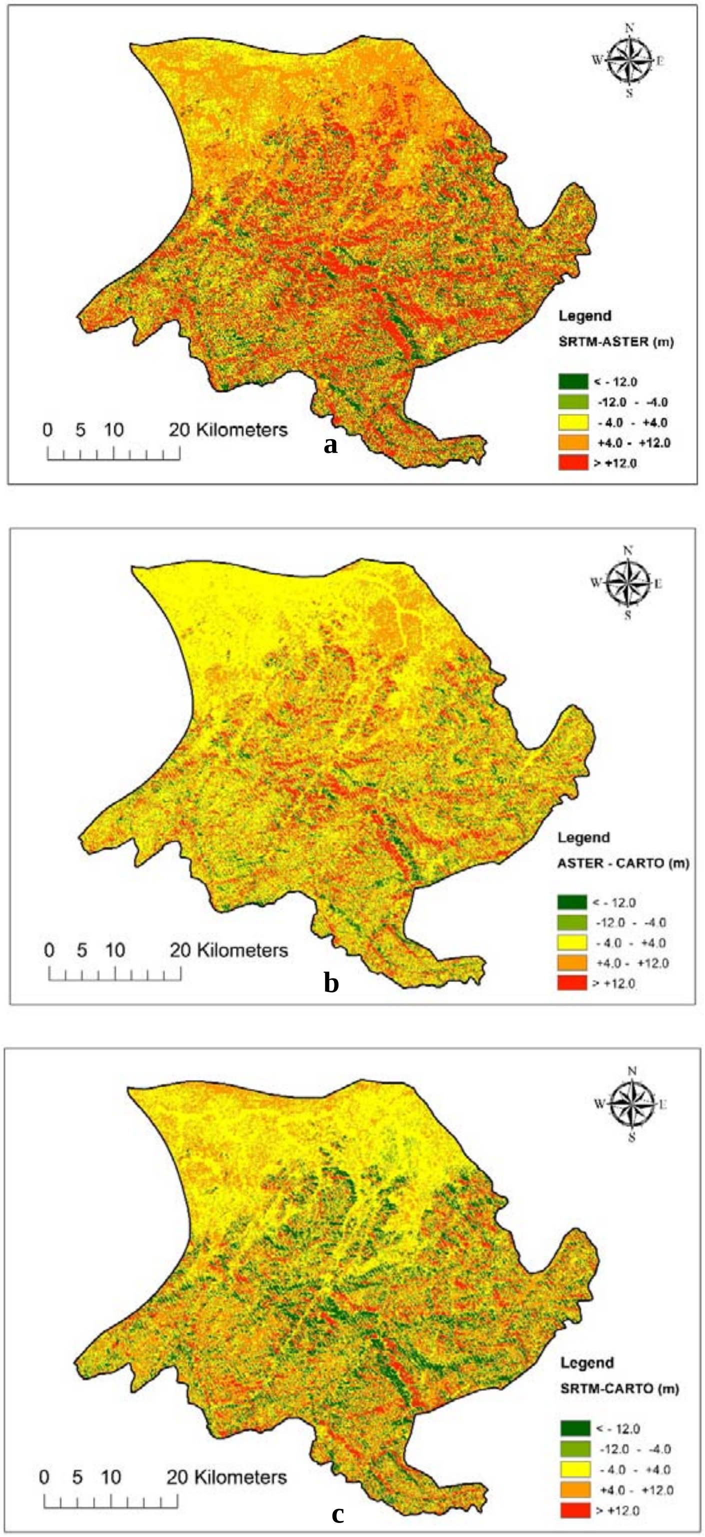

Fig 7.4 Difference in elevation between a) SRTM and ASTER (m) b) ASTER and CARTO (m) and c) SRTM and CARTO (m)

Slope was computed for the DEM using *Spatial Analyst* toolbox of ArcGIS software. Figure 7.5 shows the derived slopes for all the DEM. Visual inspection of the slope maps shows that SRTM DEM generally produces higher slope values which extend into the flood plain followed by ASTER and CARTO DEM respectively. The higher slope values signify that velocity of flow will be higher which in turn will produce higher simulated discharge values. Slope being a primary driving component in any hydrologic model regulates the runoff behaviour in the basin. The differences in the values and spatial differences of the slopes, highlights the difference in hydrologic response obtained using different DEM.

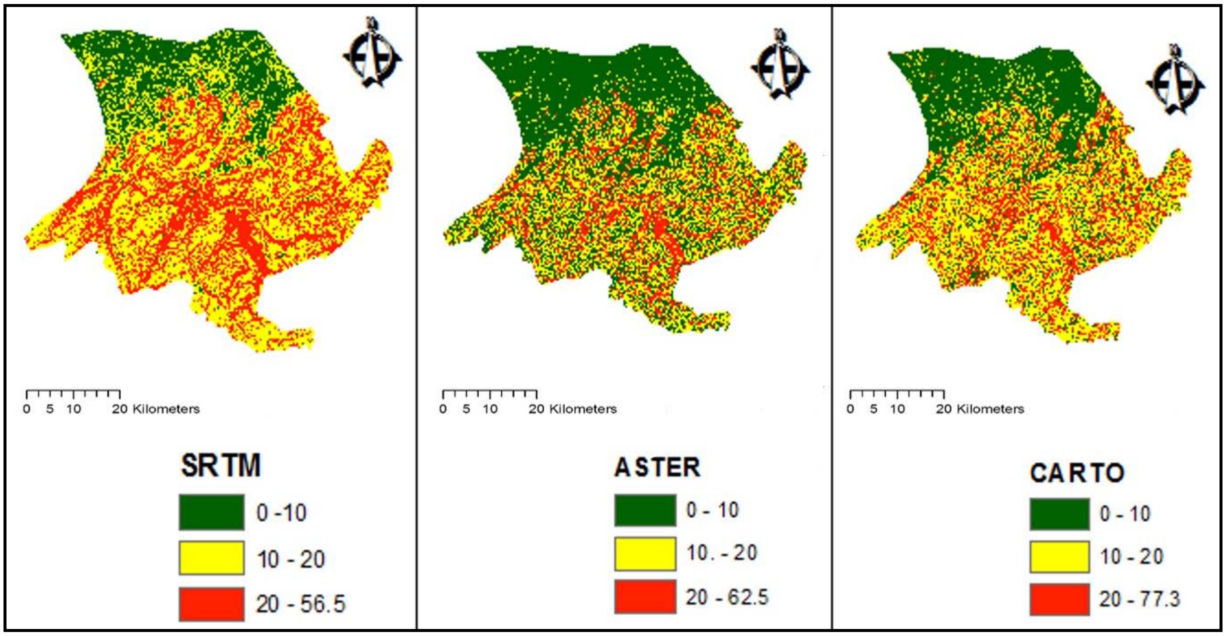

Fig 7.5 Slope of DEM used in the study

Watersheds delineated using derived flow direction from different DEM also exhibited differences in spatial extent (Figure 7.6) especially near the outlet of the basin. Watershed area of 24846.5, 25017.6 and 25187.7 km^2 was obtained using SRTM, ASTER and CARTO DEM respectively.

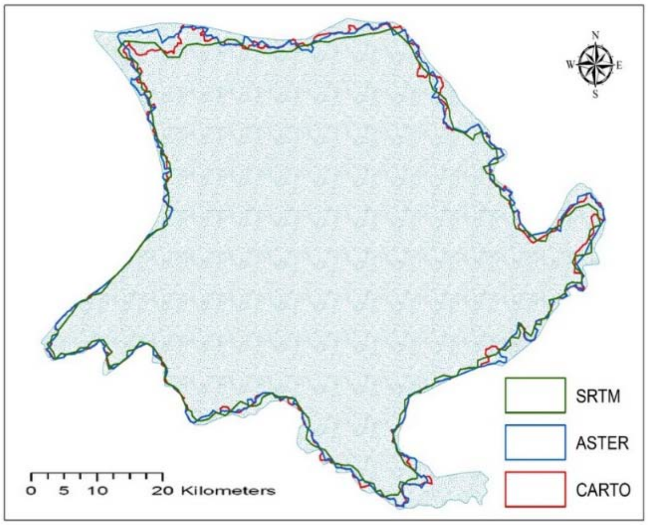

Fig 7.6 Comparison of delineated watershed obtained using different DEM

7.2Calibration of RRI model for simulation of discharge

Calibration of the RRI model was done using 2007 (May to October) flood events recorded in the Kulsi River Basin. The hydrograph at Kulsi Bazzar, which is the outlet of Kulsi River basin was used to calibrate the RRI Input parameters. Input parameters were tweaked until the simulated hydrograph matched with observed hydrograph. The performance of RRI model for different input conditions are discussed in this section. To identify the suitable soil type representing the Kulsi River Basin, the infiltration parameters in the RRI input file were change corresponding to all the soil type and simulated hydrograph was compared with the actual hydrograph (Figure 7.7).

Based on the figure it can be observed that for all the soil types the simulated hydrographs takes about 101 days to start peaking despite observing rainfall from 51 days. This result can be attributed to the time required by RRI infiltration parameters to be initialized before it can start simulating. This model behavior was found consistent for all the soil types and resulted in lowering the overall efficiency of RRI model simulation. The major peaks were simulated quite well, but RRI model simulation failed to capture the intermediate and low rising peaks of the hydrograph. The simulated hydrograph tends to overestimate thepeak values.

The performance of RRI model was quantified using three indices, Nash Sutcliff Model Efficiency (NSE), Correlation Coefficient (r^2) and Root Mean Square Error (RMSE). Table 7.4 shows

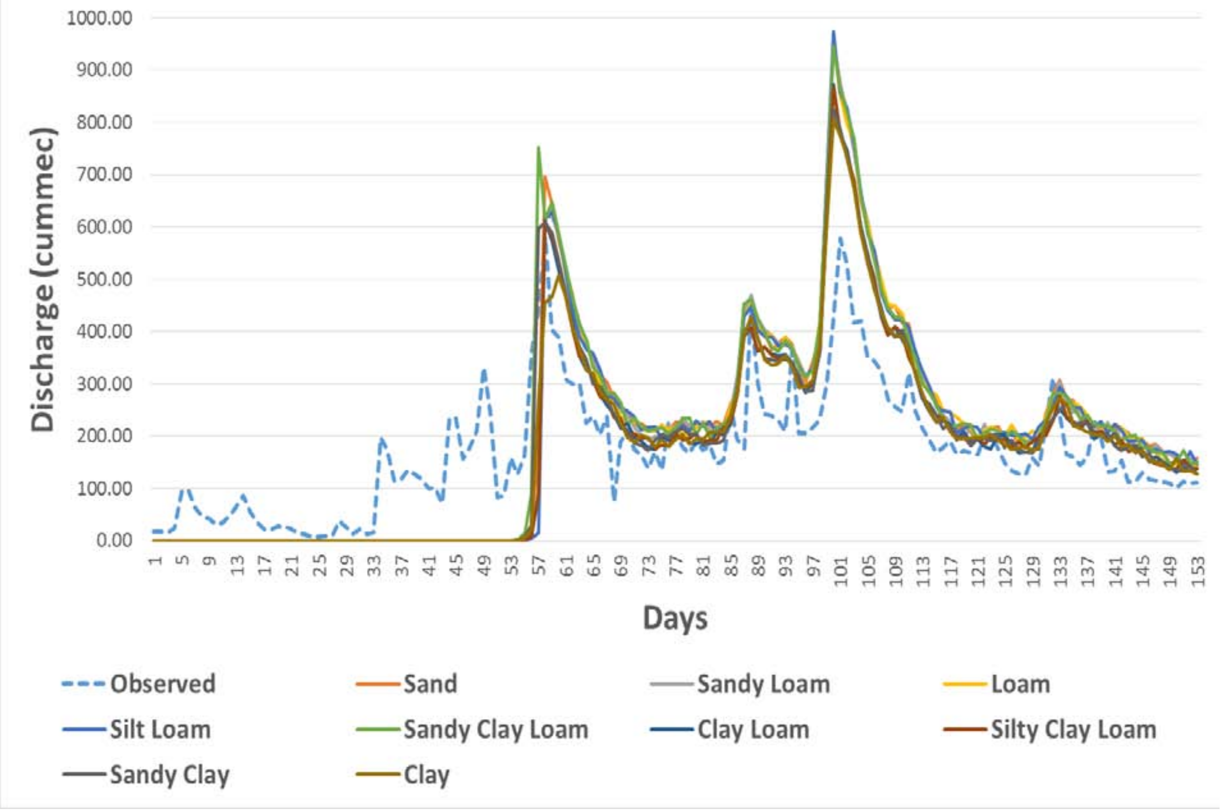

Fig 7.7Comparative performance of RRI simulation for different Soil type

Table 7.4Performance indices of RRI simulation using different soil type

Soil Type	NSE	RMSE	r^2
Sand	0.457	92.602	0.854
Sandy Loam	0.438	94.134	0.848
Loam	0.436	94.321	0.847
Silty Loam	0.391	98.002	0.822
Sandy Clay Loam	0.461	92.260	0.872
Clay Loam	0.436	94.331	0.847
Silty Clay Loam	0.435	94.403	0.847
Sandy Clay	0.472	91.282	0.869
Clay	**0.513**	**87.701**	**0.866**

the performance indices of RRI simulation using different soil types. Clay type soil was observed to be the best soil type yielding highest NSE, r^2 and lowest RMSE compared to other soil types. This soil type is predominant in the Assam and Meghalaya State region and hence can be selected to represent the soil type of Kulsi River Basin. Further calibration was performed by using clay type soil.

7.3 Sensitivity of Manning's roughness coefficient on hydrologic simulations

Manning's n values were varied between the highest and lowest values prescribed by RRI manual in order to observe the impact on discharge and inundation area simulated by RRI model. This section discusses the impact of changing manning's n on hydrologic simulations for different DEM.

7.3.1 Sensitivity of n values with SRTM DEM on hydrologic simulation

Figure 7.8 shows the variation in simulated discharge from RRI model by varying n from 0.15 to 1.0. The best fit of simulated values with observed discharge values was observed for value of n = 0.4. From the figure it can be observed that decreasing n values result in increase in discharge values. Flood peaks show higher rate of change due to changes in manning's n values compared to intermediate discharge values. Generally it was observed that a five percent decrease in values resulted in increasing the flood peaks by 3.35 %.

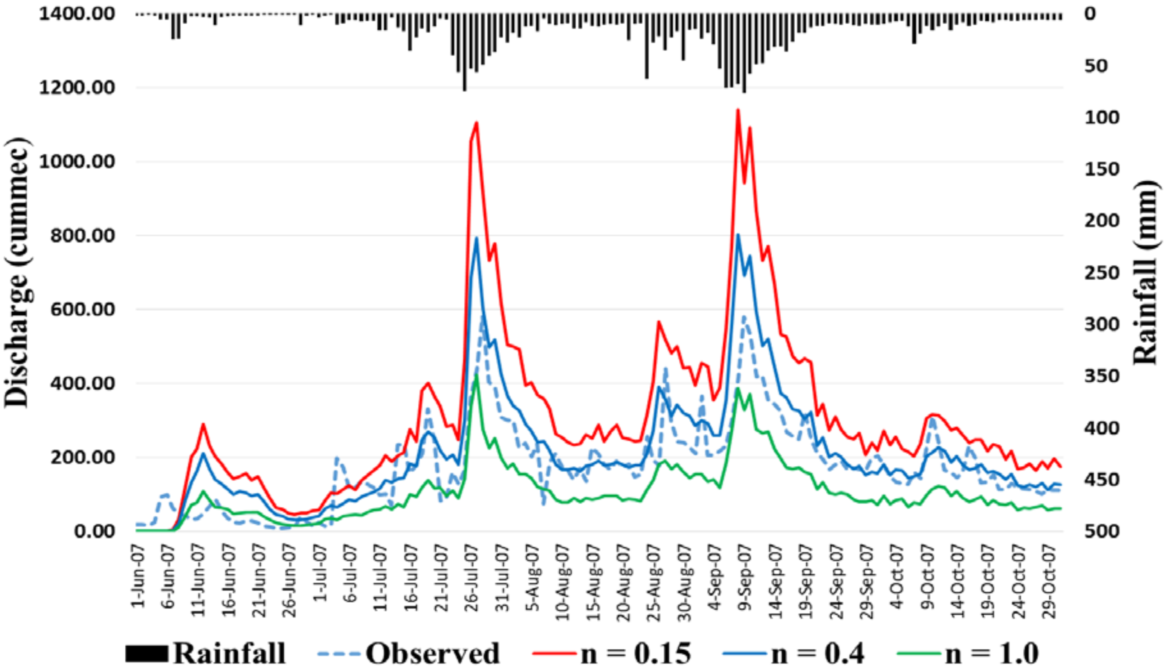

Fig 7.8 Sensitivity of Manning's n values on discharge at outlet for SRTM DEM

Table 7.5 shows the performance indices of simulated discharge and inundation area for different n values. The values of correlation coefficient do not show much variation as compared to NSE.

Table7.5 Performance of RRI model for different n values using SRTM DEM

	n = 0.15	n = 0.4	n = 1.0
NSE	-1.6562	0.4529	0.3772
r	0.8783	0.8764	0.8740
RMSE (m^3/sec)	189.8482	86.1618	91.9273
Inundation Area (km^2)	716.1893	418.5710	147.4284

and RMSE values. Variation of 64 % to 71% was observed for flood inundation area for changes in manning roughness value highlighting the highly sensitive nature of the parameter.

7.3.2 Sensitivity of n values with ASTER DEM on hydrologic simulation

Figure 7.9 shows the variation in simulated discharge from RRI model by varying n from 0.15 to 1.0 for ASTER DEM. Similar trends of changes in flood peaks were observed using ASTER DEM as in previous case. Generally it was observed that a five percent decrease in values resulted in increasing the flood peaks by 2.05 %.

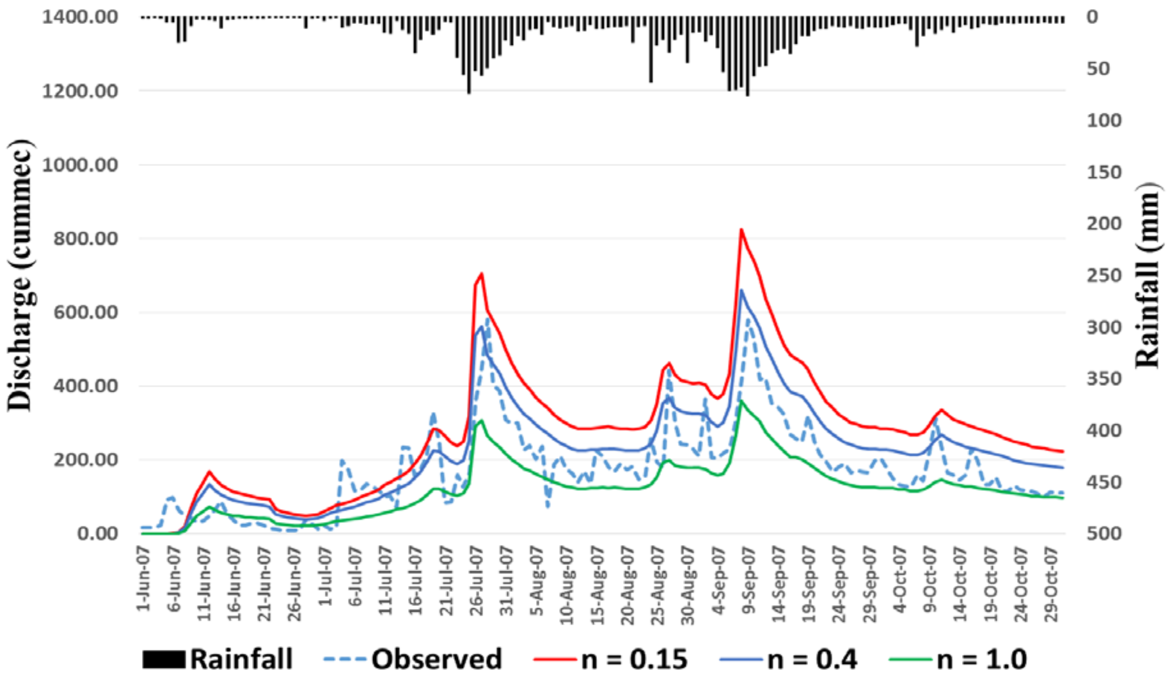

Fig 7.9 Sensitivity of Manning's n values on discharge at outlet for ASTER DEM

Table 7.6 shows the performance indices of simulated discharge and inundation area for different n values. The range of variation of NSE and RMSE is lower for ASTER DEM compared to SRTM DEM. This indicates that RRI model performance is also dependent on the type of DEM used for modelling. Varying in inundation area was observed from 57 to 61 %.corresponding to changes in n.

Table7.6 Performance of RRI model for different n values using ASTER DEM

	n = 0.15	**n = 0.4**	**n = 1.0**
NSE	-0.3536	0.5464	0.5313
r	0.8936	0.8939	0.8938
RMSE (m^3/sec)	135.5275	78.4546	79.7525
Inundation Area (km^2)	859.5120	547.3170	209.2680

7.3.3 Sensitivity of n values with CARTO DEM on hydrologic simulation

Figure 4.10 shows the variation in simulated discharge from RRI model by varying n from 0.15 to 1.0 for CARTO DEM. It was found that a five percent decrease in values resulted in increasing the flood peaks by 2.73 %. Among the DEM, SRTM DEM exhibited the highest sensitivity for changes in n values followed by ASTER and CARTO DEM respectively.

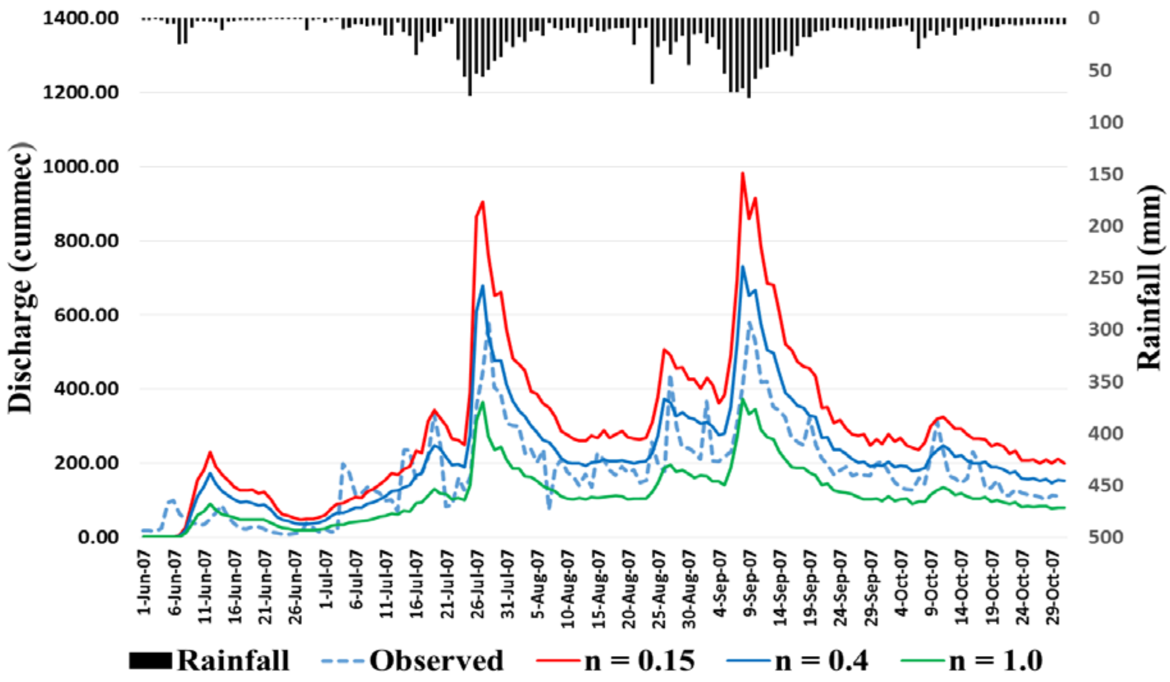

Fig 7.10 Sensitivity of Manning's n values on discharge at outlet for CARTO DEM

Table 7.7 shows the performance indices of simulated discharge and inundation area for different n values. Varying in inundation area was observed from 60 to 70 % corresponding to changes in manning's n values. The range of variation of performance indices was observed to be higher than ASTER DEM but lower than SRTM DEM.

Table7.7 Performance of RRI model for different n values using CARTO DEM

	n = 0.15	**n = 0.4**	**n = 1.0**
NSE	-0.8601	0.5471	0.4697
r	0.8966	0.8955	0.8953
RMSE (m^3/sec)	158.8706	78.3920	84.8283
Inundation Area (km^2)	773.2637	453.6810	179.7948

7.4 Sensitivity of Soil depth on hydrologic simulations

After fixing the manning's n values, soil depth parameter in RRI model was varied based on the specification from RRI manual. The soil type selected was clay as it yielded the best performance among all the other soil types as discussed in previous section. The value of soil depth was d = 0.5 m to d = 2.0 m and the effect on hydrologic simulation was observed. The following section discusses the sensitivity of soil depth using different DEM using RRI model simulations.

7.4.1 Sensitivity of soil depth with SRTM DEM on hydrologic simulation

Figure 7.11 shows the variation in simulated discharge from RRI model by varying soil depth from lowest value of d = 0.15 m to best fit for d = 1.5 to highest recommended value of d = 2.0 m. From the figure it can be observed that decreasing d values result in increase in discharge values. The range of variation of flood peaks is lower than peak variation observed for changing in manning’s n value showing that discharge values are less sensitive to soil depth variation compared to manning’s n value.

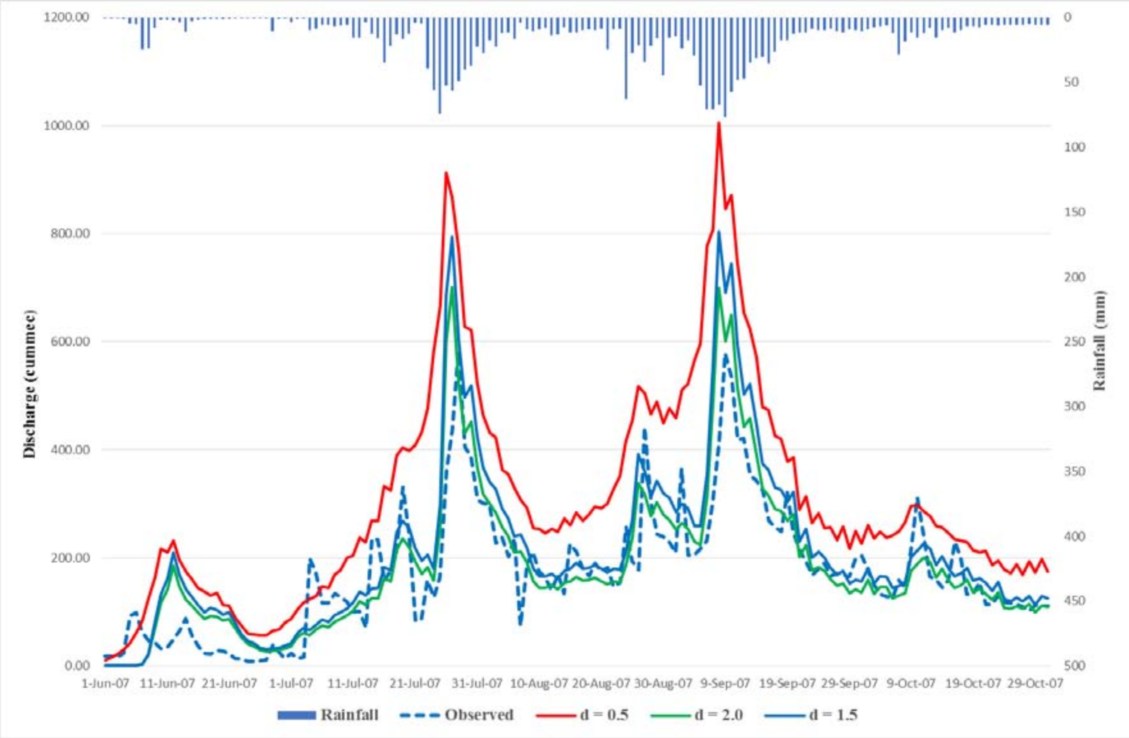

Fig 7.11 Sensitivity of soil depth values on discharge at outlet for SRTMDEM

Table 7.8 shows the performance indices of simulated discharge and inundation area for different soil depth values. Variation in inundation area was observed from 20 to 25 % corresponding to changes in soil depth values. The small range of variation of inundation area followed the same trend exhibited by the variation in discharge values.

Table7.8 Performance of RRI model for different soil depth values using SRTM DEM

	d = 0.5 m	d = 1.5 m	d = 2.0 m
NSE	-1.3906	0.4529	0.3751
r	0.8414	0.8764	0.8159
RMSE (m^3/sec)	180.1061	86.1618	96.3921
Inundation Area (km^2)	524.2223	418.571	332.9942

7.4.2 Sensitivity of soil depth with ASTER DEM on hydrologic simulation

Figure 7.12 shows the variation in simulated discharge from RRI model by varying soil depth values. Changing the values of soil depth by 5 % results in variation of discharge peaks by 1.7 % for ASTER DEM. Maximum flood peaks are mimicked quite well for all the soil depth however the intermediate peaks are not simulated well which could be result of limitation of the data or RRI model used.

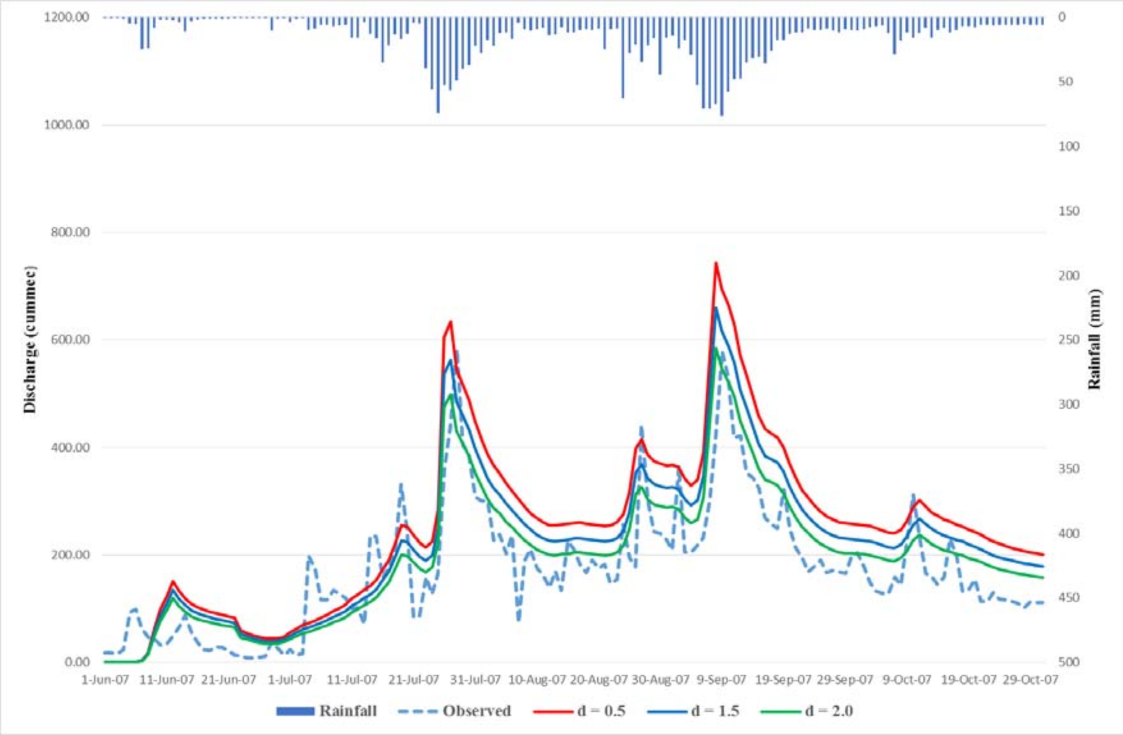

Fig 7.12 Sensitivity of soil depth values on discharge at outlet for ASTER DEM

Table 7.9 shows the performance indices of simulated discharge and inundation area for different soil depth values for ASTER DEM. The values of NSE were observed to vary from 0.1778 (d = 0.5 m) to 0.5464 m (d = 1.5 m). Simulated flood inundated area by RRI model was found to vary from 7.2 % to 27.8 %.

Table7.9 Performance of RRI model for different soil depth values using ASTER DEM

	d = 0.5 m	d = 1.5 m	d = 2.0 m
NSE	0.1778	0.5464	0.3753
r	0.8937	0.8939	0.7939
RMSE (m^3/sec)	105.6225	78.4546	89.6779
Inundation Area (km^2)	696.6678	547.317	506.1732

7.4.3 Sensitivity of soil depth with CARTO DEM on hydrologic simulation

Figure 7.13 shows the variation in simulated discharge from RRI model by varying soil depth values for CARTO DEM. Changing the values of soil depth by 5 % results in variation of discharge peaks by 0.6 % for ASTER DEM.

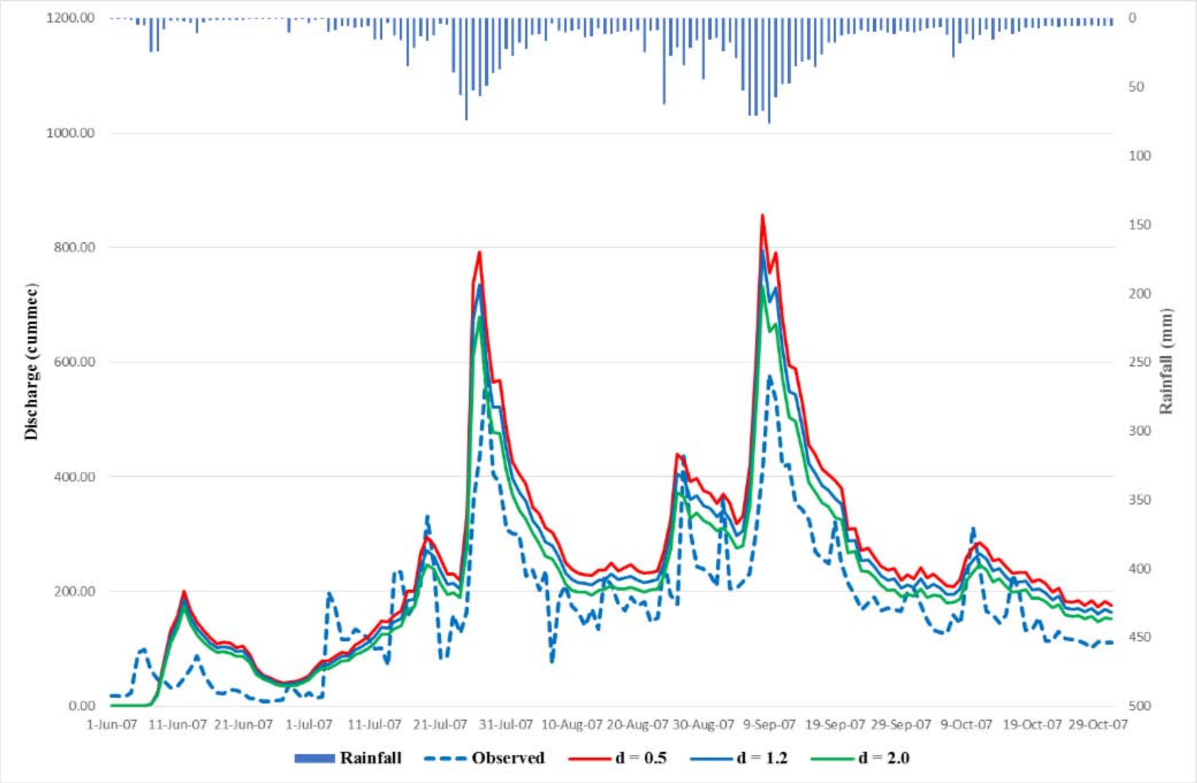

Fig 7.13 Sensitivity of soil depth values on discharge at outlet for CARTO DEM

Table 7.10 shows the performance indices of simulated discharge and inundation area for different soil depth values for CARTO DEM. The values of RMSE were observed to vary from 79.48 m^3/s (d = 1.5 m) to 116.48 m^3/s (d = 0.5 m). Simulated flood inundated area by RRI model was found to vary from 11.43 % to 13.49 % for changes in soil depth.

Table7.10 Performance of RRI model for different soil depth values using CARTO DEM

	d = 0.5 m	**d = 1.5 m**	**d = 2.0 m**
NSE	-0.0247	0.5344	0.4429
r	0.8963	0.8955	0.7560
RMSE (m^3/sec)	116.4877	79.4849	99.0690
Inundation Area (km^2)	514.8834	453.681	401.8219

7.5 Sensitivity of smoothing of DEM on hydrologic simulations

After calibrating RRI model with manning's n values and soil depth parameter, the effect of different smoothing filters of DEM on hydrologic simulations were observed. Four types of filters i.e. low pass filter, enhanced lee filter (window size = 3), enhanced lee filter (window size = 5) and denoising algorithms were applied to SRTM, ASTER and CARTO DEM respectively. The following section discusses the sensitivity of smoothing filters of different DEM using RRI model simulations.

7.5.1 Sensitivity of smoothing of SRTM DEM on hydrologic simulation

Figure 7.13 shows the variation in simulated discharge from RRI model by using different smoothing filters for SRTM DEM. Low pass filter generally resulted in simulation of higher discharge values. Denoising algorithm resulted in simulation of lowest discharge values closer to the observed hydrograph.

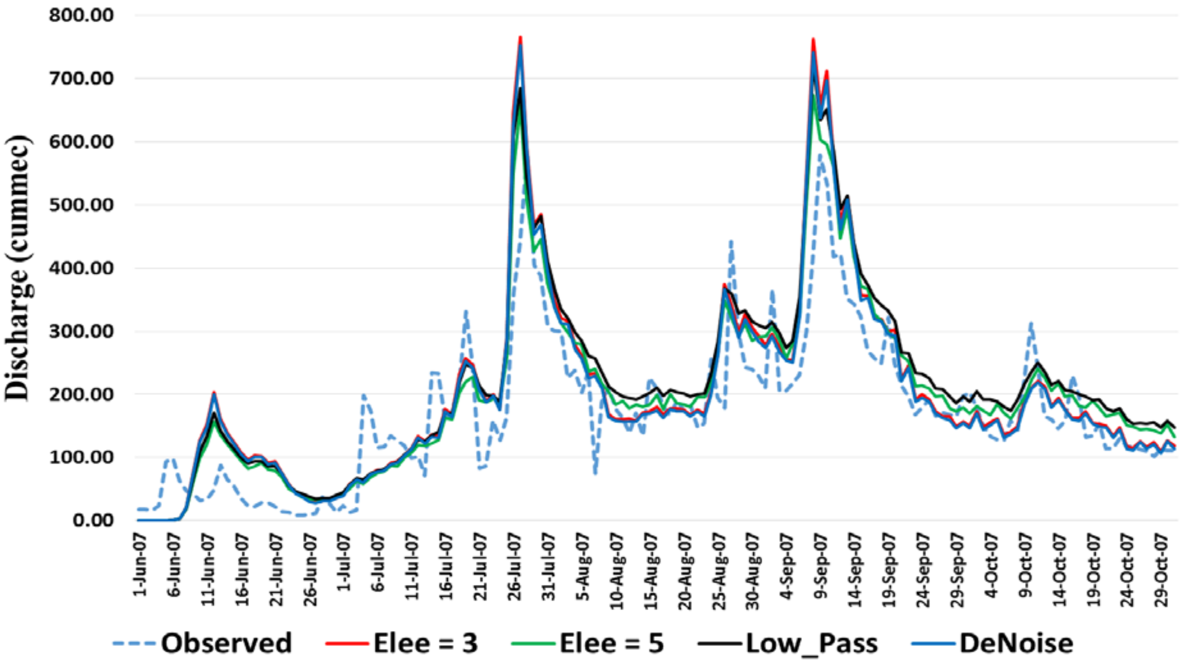

Fig 7.14 Sensitivity of smoothing of SRTM DEM on discharge at outlet

Table 7.11 shows the performance indices of simulated discharge for different smoothing filters for SRTM DEM. The values of RMSE were observed to vary from 71.92 m^3/s (denoising algorithm) to 79.36 m^3/s (low pass filter). Increasing the window size from 3 to 5 of enhanced lee filter resulted decrease in performance indices, which signifies the importance of selecting proper filter size for DEM. NSE values were observed to increase by 29 % and RMSE values decreased by 13 % on comparison of performance of SRTM DEM with and without smoothing filters. Denoising algorithm resulted in the best performance (NSE = 0.5844, RMSE = 71.92) among all the filters.

Table7.11 Performance of RRI model for smoothing of SRTM DEM

	Low Pass Filter	Lee Filter (window size = 3)	Lee Filter (window size = 5)	Denoising Algorithm
NSE	0.5358	0.5453	0.5188	0.5844
r	0.8752	0.8772	0.8769	0.8780
RMSE (m^3/sec)	79.3609	75.0946	78.5472	71.9247

7.5.2 Sensitivity of smoothing of ASTER DEM on hydrologic simulation

Figure 7.15 shows the variation in simulated discharge from RRI model by using different smoothing filters for ASTER DEM. Low pass filter generally resulted in simulation of lower discharge values. Enhanced lee filter with window size 3 produced the highest peak and variation of simulated discharge. Denoising algorithm resulted in simulation of lowest discharge values closer to the observed hydrograph.

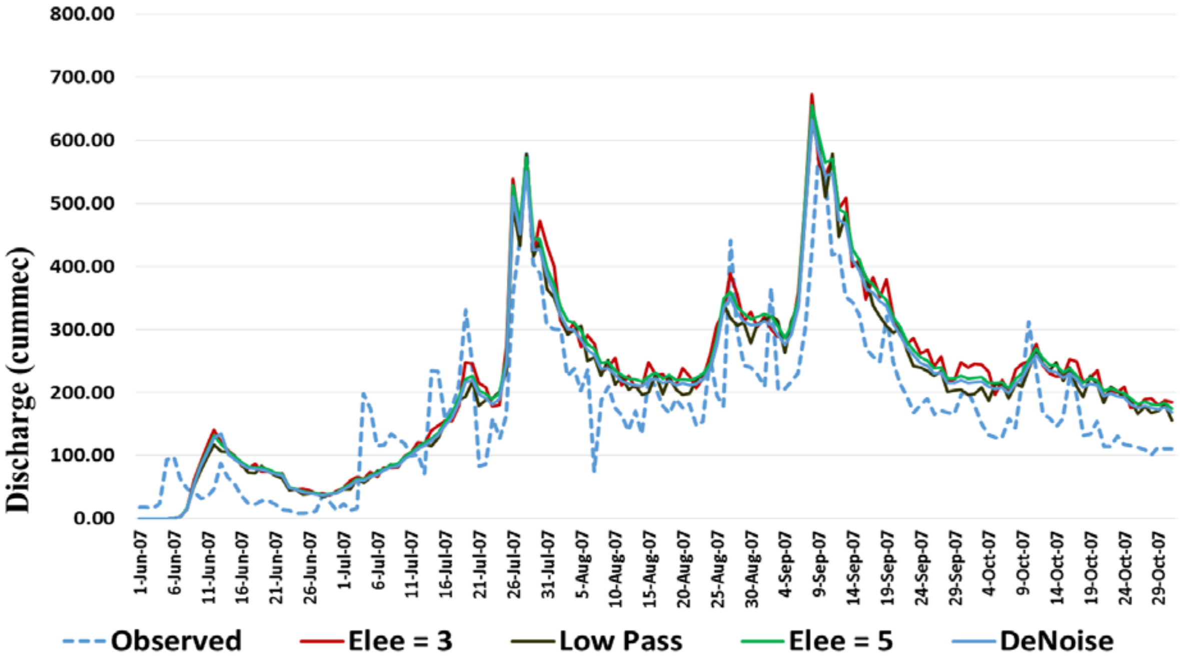

Fig 7.15 Sensitivity of smoothing of ASTER DEM on discharge at outlet

Table 7.12 shows the performance indices of simulated discharge for different smoothing filters for ASTER DEM. NSE values were observed to increase by 16% and RMSE values decreased by 14 %

on comparison of performance of ASTER DEM with and without smoothing filters. Denoising algorithm resulted in the best performance (NSE = 0.6342, RMSE = 67.39) among all the filters.

Table7.12 Performance of RRI model for smoothing of ASTER DEM

	Low Pass Filter	Lee Filter (window size = 3)	Lee Filter (window size = 5)	Denoising Algorithm
NSE	0.5615	0.6290	0.5448	0.6342
r	0.8886	0.8921	0.8916	0.9023
RMSE (m^3/sec)	77.1397	70.4515	78.5875	67.3880

7.5.3 Sensitivity of smoothing of CARTO DEM on hydrologic simulation

Figure 7.16 shows the variation in simulated discharge from RRI model by using different smoothing filters for CARTO DEM. Low pass filter generally resulted in simulation of higher discharge values for major peaks, while enhanced filter with window size 5 resulted in higher discharge values for the intermediate peaks. Denoising algorithm resulted in simulation of lowest discharge values closer to the observed hydrograph.

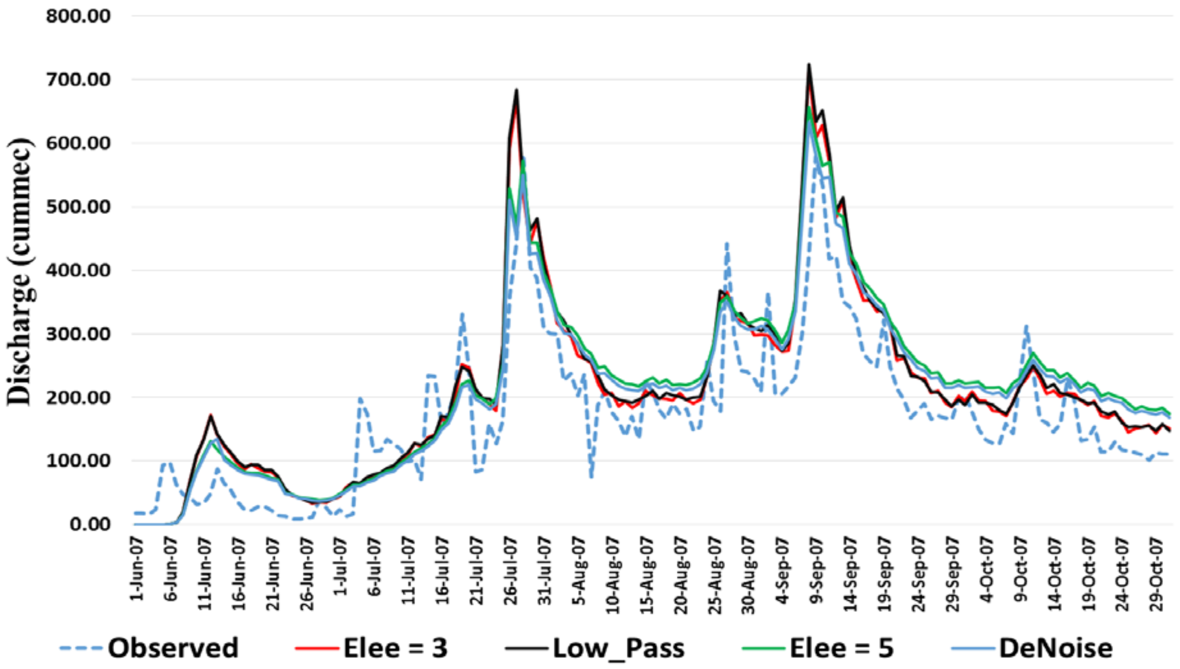

Fig 7.16 Sensitivity of smoothing of CARTO DEM on discharge at outlet

Table 7.13 shows the performance indices of simulated discharge for different smoothing filters for CARTO DEM. NSE values were observed to increase by 13% and RMSE values decreased by 9 % on comparison of performance of CARTO DEM with and without smoothing filters. Denoising algorithm resulted in the best performance (NSE = 0.6234, RMSE = 70.95) among all the filters.

Table7.13 Performance of RRI model for smoothing of CARTO DEM

	Low Pass Filter	**Lee Filter (window size = 3)**	**Lee Filter (window size = 5)**	**Denoising Algorithm**
NSE	0.5575	0.5961	0.6153	0.6234
r	0.8909	0.8951	0.8949	0.8954
RMSE (m^3/sec)	77.4850	74.0315	71.4883	70.9479

7.6 Validation of RRI model for simulation of discharge

Validation of the RRI model was done using 2008 (June to August) flood events recorded in the Kulsi River Basin. RRI model was run using the calibrated input parameters to simulate the hydrograph at Kulsi Bazzar. The performance of RRI model for DEM with and without smoothing filters is discussed in this section.

7.6.1 Validation of RRI model for simulation of discharge using SRTM DEM

Figure 7.17 shows the validation results for simulated discharge from RRI model by using different smoothing filters for SRTM DEM. Dem without smoothing filter resulted in slightly higher values of discharge simulation compared to DEM with smoothing. Variation of simulated discharge was higher for major peaks compared to simulated discharge for the intermediate peaks. Denoising algorithm resulted in simulation of lowest discharge values closer to the observed hydrograph.

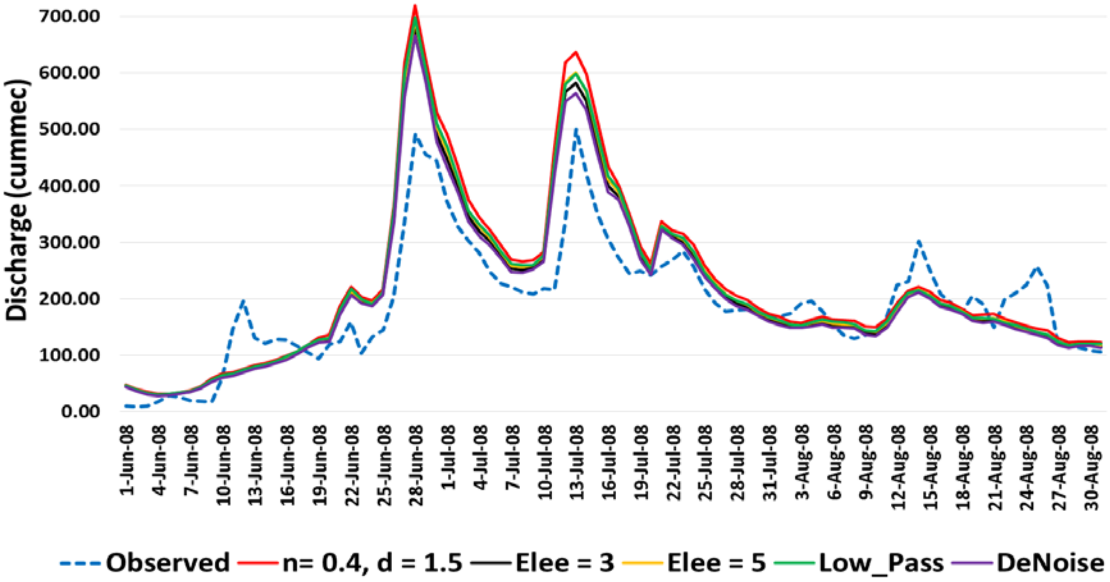

Fig 7.17 Validation of RRI model for SRTM DEM on discharge at outlet

Table 7.14 shows the performance indices of simulated discharge for validation data using SRTM DEM. Performance indices of SRTM DEM with smoothing was higher than without smoothing emphasizing the importance of smoothing filters. Denoising algorithm resulted in the best performance among all the filters. NSE values were observed to increase from 0.267 to 0.5039 and RMSE values decreased from 108.1 m^3/sec to 87.9 m^3/sec on comparison of performance of CARTO DEM with and without smoothing filters.

Table7.14 Performance of RRI model for validation using SRTM DEM

	Without Smoothing	Low Pass Filter	Lee Filter (size = 3)	Lee Filter (size = 5)	Denoising Algorithm
NSE	0.267	0.382	0.4548	0.3989	0.5039
r	0.875	0.8748	0.8759	0.8755	0.8762
RMSE (m^3/sec)	108.1	98.8602	92.5243	97.4341	87.9517

7.6.2 Validation of RRI model for simulation of discharge using ASTER DEM

Figure 4.18 shows the validation results for simulated discharge from RRI model by using different smoothing filters for ASTER DEM. Variation of simulated discharge was higher for major peaks compared to simulated discharge for the intermediate peaks. ASTER DEM smoothened using low pass filter resulted in highest simulations. Denoising algorithm resulted in simulation of lowest discharge values closer to the observed hydrograph.

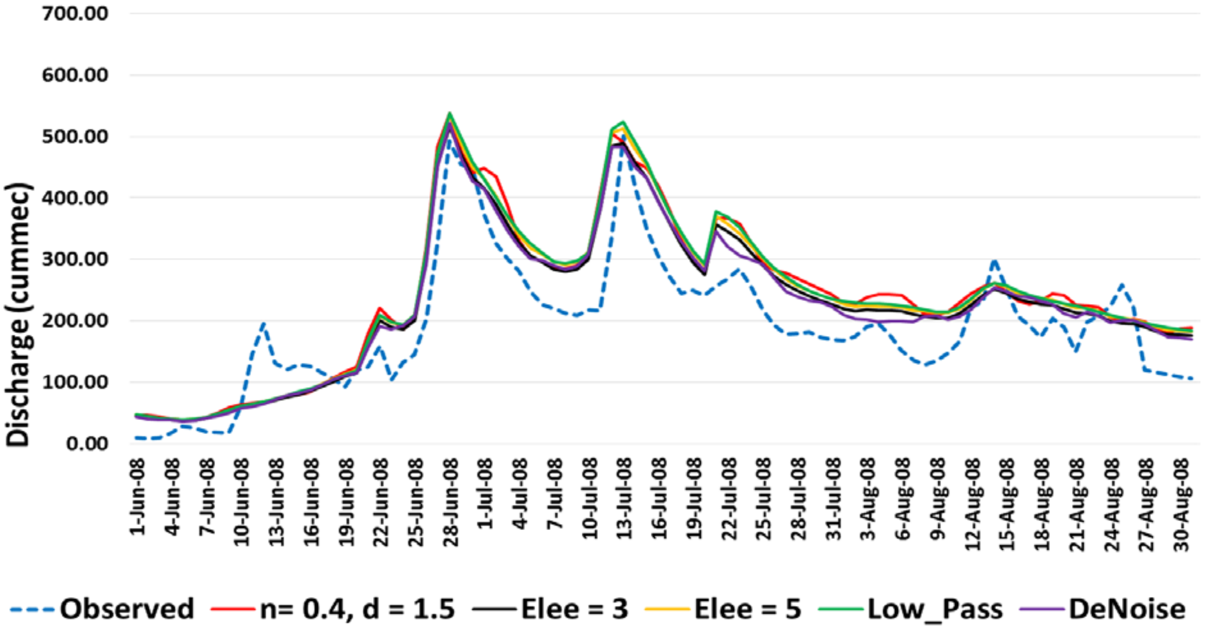

Fig 7.18 Validation of RRI model for ASTER DEM on discharge at outlet

Table 7.15 shows the performance indices of simulated discharge for validation data using ASTER DEM. Performance indices of ASTER DEM with smoothing was higher than without smoothing. Denoising algorithm resulted in the best performance among all the filters and all the DEM. NSE values were observed to increase from 0.4327to 0.5831 and RMSE values decreased from 94.5 m^3/sec to 79.9 m^3/sec on comparison of performance of CARTO DEM with and without smoothing filters.

Table7.15 Performance of RRI model for validation using ASTER DEM

	Without Smoothing	**Low Pass Filter**	**Lee Filter (size = 3)**	**Lee Filter (size = 5)**	**Denoising Algorithm**
NSE	0.4327	0.4394	0.5589	0.464	0.5831
r	0.8792	0.8881	0.8874	0.8875	0.8884
RMSE (m^3/sec)	94.5035	93.9025	82.4796	91.6879	79.9413

7.6.3 Validation of RRI model for simulation of discharge using CARTO DEM

Figure 7.19 shows the validation results for simulated discharge from RRI model by using different smoothing filters for CARTO DEM. Variation of simulated discharge was higher for major peaks compared to simulated discharge for the intermediate peaks. CARTO DEM smoothened using low pass filter resulted in highest simulations. Denoising algorithm resulted in simulation of lowest discharge values closer to the observed hydrograph.

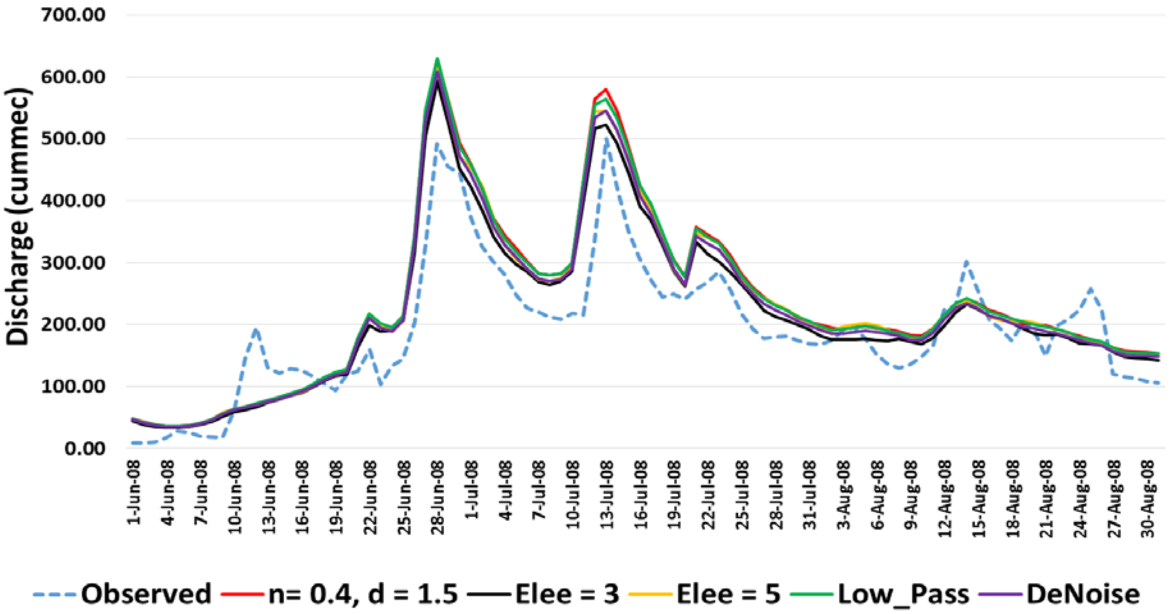

Fig 7.19 Validation of RRI model for CARTO DEM on discharge at outlet

Table 7.16 shows the performance indices of simulated discharge for validation data using CARTO DEM. Performance indices of CARTO DEM with smoothing was higher than without smoothing. Denoising algorithm resulted in the best performance among all the filters. NSE values were observed to increase from 0.4205 to 0.5253 and RMSE values decreased from 95.6 m^3/sec to 79.5 m^3/sec on comparison of performance of CARTO DEM with and without smoothing filters.

Table7.16 Performance of RRI model for validation using CARTO DEM

	Without Smoothing	**Low Pass Filter**	**Lee Filter (size = 3)**	**Lee Filter (size = 5)**	**Denoising Algorithm**
NSE	0.4205	0.4342	0.497	0.4632	0.5253
r	0.8713	0.8805	0.8917	0.8892	0.893
RMSE (m^3/sec)	95.5659	94.3665	85.8713	89.6216	79.4285

7.7 Simulation of flood extent using RRI model

Inundation area was simulated using RRI model for calibration and validation data. The output from RRI model was exported into ArcGIS. MLSWI was computed for the MODIS imagery of the corresponding period and flood and non–flood area were differentiated. A threshold value of 0.65 was used in order to differentiate the flood and non- flood area from MLSWI. The inundation area simulated from RRI was compared with inundation area derived from MLSWI of MODIS imagery and results are discussed in this section.

7.7.1 Comparison of simulated flood extent with MODIS imagery for 2007 flood

Inundation area for 28-07-2007 was computed using RRI model for DEM with and without smoothing and results compared with MLSWI derived from MODIS Imagery. Table 7.17 shows the comparison of inundation area simulated by RRI model. Inundation area derived from MODIS imagery for the period was calculated to be 746.83 km^2.

Table7.17Comparison of simulated flood extent with MODIS imagery for 2007 flood

Source of DEM	Inundation Area (km^2)				
	Without Smoothing	Low Pass Filter	Lee Filter (size = 3)	Lee Filter (size = 5)	Denoising Algorithm
SRTM	418.57	429.36	429.57	436.15	485.55
ASTER	547.31	556.04	574.77	596.45	615.86
CARTO	453.68	455.57	463.43	484.41	509.51

Comparison of inundation area shows that RRI model using ASTER DEM were closer to those derived from MODIS imagery. Inundation area simulated using RRI model with SRTM DEM showed the least extent among DEM. CSI between RRI model and MODIS imagery produced a value of 0.47, 0.57 and 0.51 respectively for SRTM, ASTER and CARTO DEM respectively. It is observed that RRI model generally underestimate the simulated flood extent compared to MODIS imagery. The combination of denoising algorithm with ASTER DEM produced inundation area of 615.86 km^2, which was closest to flood extent derived from MODIS imagery.

7.7.2Comparison of simulated flood extent with MODIS imagery for 2008 flood

Inundation area for 13-06-2008 was computed using RRI model for DEM with and without smoothing and results compared with MLSWI derived from MODIS Imagery. Table 7.18 shows the comparison of inundation area simulated by RRI model. Inundation area derived from MODIS imagery for the period was calculated to be 560.09 km^2.

Table7.18 Comparison of simulated flood extent with MODIS imagery for 2008 flood

Source of DEM	Inundation Area (km^2)				
	Without Smoothing	Low Pass Filter	Lee Filter (size = 3)	Lee Filter (size = 5)	Denoising Algorithm
SRTM	310.76	279.66	262.20	260.69	364.18
ASTER	433.83	377.13	431.03	442.94	450.95
CARTO	348.68	306.21	382.36	304.41	366.25

Comparison of inundation area shows that RRI model using ASTER DEM were closer to those derived from MODIS imagery.CSI between RRI model and MODIS imagery produced a value of 0.45, 0.47 and 0.44 respectively for SRTM, ASTER and CARTO DEM respectively. The combination of denoising algorithm with ASTER DEM produced inundation area of 450.95 km^2, which was closest to flood extent derived from MODIS imagery. Figure 7.20 shows the difference in spatial distribution of flooded area in the flood plain simulated by best performing combination of DEM and smoothing of RRI model with MODIS imagery. Maximum inundation is observed around the river bend and near the outlet in the flood plains.

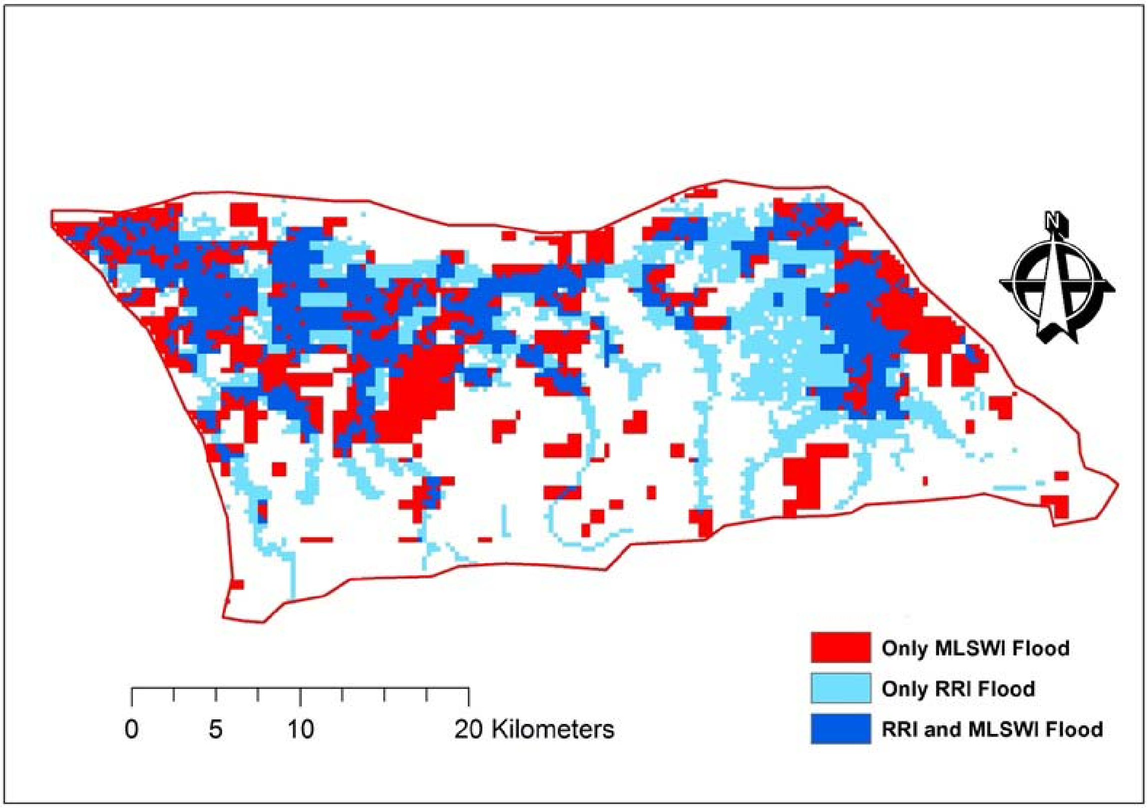

Fig 7.20 Comparison of the best performing RRI model (ASTER DEM + Denoising algorithm) with MODIS derived MLSWI

8. DISCUSSION

The results of this study showed remarked variations among different DEM characterizing the topography in the basin. The quality of topographic data is dependent on several factors such as sampling density, data acquisition, spatial resolution and interpolation algorithm used to generate the DEM and terrain characteristics.

Determination of absolute accuracy of DEM based on DGPS showed different patterns for low lying area, and gently rolling and steep slope areas in the basin. The presence of thick forest along the gently rolling topography of the basin might have increased errors of DEM due to the backscattering of signals from different satellite sensors, which was more prominently seen for SRTM DEM for this study.

Relative accuracy of DEM, derived by pixel to pixel comparison showed uniform differences in the flat regions among DEM. The highest magnitude differences appeared to be distributed along the steep slopes following the stream network in the basin.

DEM derived slope from DEM revealed that the steepest slopes was underestimated for SRTM DEM compared to ASTER and CARTO DEM. SRTM DEM produced higher slopes in the flood plain compared to ASTER and CARTO DEM. This pattern explains the consistent over estimation using RRI model for discharge measured at the outlet.

Among the DEM, SRTM DEM showed minimum watershed area compared to the hydrological boundary of the basin. This pattern gets replicated in RRI simulations of flood inundation extent using SRTM DEM. The moderate resolution of raw SRTM data compared to ASTER and CARTO DEM is unable to capture the variation in flow direction, especially near the outlet of the basin.

We found that selection of parameters of smoothing algorithm influenced the hydrologic simulations seen in the case of enhanced lee filter. Enhanced lee filter of 3 by 3 window improved the performance of RRI simulations compared to enhanced lee filter of 5 by 5 window.

. The simulation of flood extent by RRI model was consistent along the river network, while MODIS imagery showed patchy inundation area. The reason for this could be attributed to the low spatial resolution of MODIS imagery and the limitation of MODIS in presence of mixed areas within the pixel and limitation of index adopted to differentiate flood and non-flood area.

9. CONCLUSIONS

The following conclusions of the study have been drawn:

i. Comparison with DGPS point elevations, SRTM DEM produced least error in flood plains, however for forest and hilly areas, the best result was obtained from ASTER DEM.

ii. Sensitivity analysis showed that RRI model is highly sensitive to Manning's *n* values for flood plain, followed with source of DEM and soil depth among the input parameters.

iii. Calibration and validation of RRI model reproduced the maximum flood peaks quite well.

iv. The simulated inundation extent was more influent by topography modified smoothing filters than its simulated discharge at the outlet of the basin.

v. Denoising algorithm performed better among other smoothing filters of DEM for hydrologic simulations.

10. RECOMMENDATIONS FOR FUTURE STUDIES

Following the results obtained in this study, limitations/challenges faced during the study, the following recommendations are made for future studies:

i. Checking the performance of discharge not only at the outlet point but also at the upstream points in the basin.

ii. Although absolute vertical accuracy of DEM were evaluated in this study, the comparison of relative elevation accuracy of the DEM with high resolution topographic maps will further useful in determining their suitability for hydrologic simulations. One such maps are available from Advanced Land Observing Satellite (ALOS) of 5 m by 5 m spatial resolution are from Japan Aerospace Exploration Agency (JAXA).

iii. Uncertainty analysis of DEM using Monte Carlo simulations on RRI model simulations will be beneficial in quantifying the impact of using different topographic data.

iv. Inclusion of evapotranspiration, river cross section data, base flow and interaction of ground water with surface water will enhance the performance and reliability of RRI model.

v. Improving the best fitting parameters of smoothing filters for different resolution of on hydrologic simulation will be useful in determining the best fitting parameters required to adequately characterize the catchment behaviour.

vi. Comparison of flood inundated area with indices derived from LANDSAT imagery will increase the reliability of RRI model simulations.

11. REFERENCES

Beven, KJ, & Kirkby, MJ. (1979). A physically based, variable contributing area model of basin hydrology. *Hydrological Sciences Journal, 24*(1), 43-69.

Brandt, S Anders. (2005). *Resolution issues of elevation data during inundation modeling of river floods.* Paper presented at the XXXI IAHR CONGRESS. 11-16 september, 2005, COEX, Seoul, Korea.

Casas, A, Benito, Gerardo, Thorndycraft, VR, & Rico, Mayte. (2006). The topographic data source of digital terrain models as a key element in the accuracy of hydraulic flood modelling. *Earth Surface Processes and Landforms, 31*(4), 444-456.

Cash, Jeff R, & Karp, Alan H. (1990). A variable order Runge-Kutta method for initial value problems with rapidly varying right-hand sides. *ACM Transactions on Mathematical Software (TOMS), 16*(3), 201-222.

Central Water Commission. (1996). Report of the Working Group on Flood Management for the 9th five year plan (1997–2002), CWC, New Delhi.

Clarenz, Ulrich, Diewald, Udo, & Rumpf, Martin. (2000). *Anisotropic geometric diffusion in surface processing.* Paper presented at the Proceedings of the conference on Visualization'00.

Cobby, David M, Mason, David C, & Davenport, Ian J. (1999). Image processing of airborne scanning laser altimetry data for improved river flood modelling. *ISPRS Journal of Photogrammetry and Remote Sensing, 56*(2), 121-138.

Cook, Aaron, & Merwade, Venkatesh. (2009). Effect of topographic data, geometric configuration and modeling approach on flood inundation mapping. *Journal of Hydrology, 377*(1), 131-142.

Desbrun, Mathieu, Meyer, Mark, Schröder, Peter, & Barr, Alan H. (2000). *Anisotropic Feature-Preserving Denoising of Height Fields and Bivariate Data.* Paper presented at the Graphics interface.

BMPTC. (1997). Expert Group Report Part–II, BMTPC, Min. of Urban Dev., Govt. of India,

Field, David A. (1988). Laplacian smoothing and Delaunay triangulations. *Communications in applied numerical methods, 4*(6), 709-712.

Global Water Partnership. (1999). The Dublin Principles for Water as Reflected in a Comparative Assessment of Institutional and Legal Arrangements for Integrated Water Resources Management (M. Solanes and F. Gonzalez-Villarreal). Technical Advisory Committee (TAC) Background Paper No. 3, Stockholm, Global Water Partnership/International Development Cooperation Agency.

Goswami, Dulal C. (2008). Fluvial Geomorphology of the Brahmaputra River, Assam: An Overview. *North-East India: geo-environmental issues*, 31.

Hewitt, K. (1997). Regions of Risk: A Geographical Introduction to Disasters, (Harlow London: Addison-Wesley Longman).

Hunter, Neil M, Bates, Paul D, Horritt, Matthew S, & Wilson, Matthew D. (2007). Simple spatially-distributed models for predicting flood inundation: a review. *Geomorphology, 90*(3), 208-225.

Ishihara, T, & Takasao, T. (1962). A study on the subsurface runoff and its effects on runoff process. *Trans. JSCE, 79*, 15-21.

Iwasa, Yoshiaki, & Inoue, Kazuya. (1982). Mathematical simulations of channel and overland flood flows in view of flood disaster engineering. *Natural disaster science, 4*(1), 1-30.

Kim, ByungMoon, & Rossignac, Jarek. (2005). *Geofilter: Geometric selection of mesh filter parameters.* Paper presented at the Computer Graphics Forum.

Kirkby, MJ. (1975). *Hydrograph modelling strategies*: Department of Geography, University of Leeds.

Manfreda, S, Sole, A, & Fiorentino, M. (2008). Can the basin morphology alone provide an insight into floodplain delineation. *WIT Trans Ecol Environ, 118*, 47-56.

Mitchell, J. K. (1999). Crucibles of Hazard: Mega-Cities and Disaster in Transition, (New York: United Nations Publication).

Moreton, Henry P, & Séquin, Carlo H. (1992). *Functional optimization for fair surface design* (Vol. 26): ACM.

Ohtake, Yutaka, Belyaev, Alexander, & Bogaevski, Ilia. (2000). Mesh regularization and adaptive smoothing. *Computer-Aided Design, 33*(11), 789-800.

Oimoen, Michael J. (2000). *An effective filter for removal of production artifacts in US Geological Survey 7.5-minute digital elevation models.* Paper presented at the Proceedings of the Fourteenth International Conference on Applied Geologic Remote Sensing.

Paiva, Rodrigo CD, Collischonn, Walter, & Tucci, Carlos EM. (2011). Large scale hydrologic and hydrodynamic modeling using limited data and a GIS based approach. *Journal of Hydrology, 406*(3), 170-181.

Patro, S, Chatterjee, C, Mohanty, S, Singh, R, & Raghuwanshi, NS. (2009). Flood inundation modeling using MIKE FLOOD and remote sensing data. *Journal of the Indian Society of Remote Sensing, 37*(1), 107-118.

Preventionweb, UNISDR; India Disaster Statistics; Website:

http://www.preventionweb.net/english/countries/statistics/?cid=79

Sayama, Takahiro, Ozawa, Go, Kawakami, Takahiro, Nabesaka, Seishi, & Fukami, Kazuhiko. (2012). Rainfall–runoff–inundation analysis of the 2010 Pakistan flood in the Kabul River basin. *Hydrological Sciences Journal, 57*(2), 298-312.

Schumann, Guy, Matgen, Patrick, Cutler, MEJ, Black, Andrew, Hoffmann, Lucien, & Pfister, Laurent. (2008). Comparison of remotely sensed water stages from LiDAR, topographic contours and SRTM. *ISPRS journal of photogrammetry and remote sensing, 63*(3), 283-296.

Singh, RD, Wheater, H, Sorooshian, S, & Sharma, KD. (2008). Real-time flood forecasting: Indian experiences. *Hydrological modelling in arid and semi-arid areas*, 139-155.

Sun, Xianfang, Rosin, Paul L, Martin, Ralph R, & Langbein, Frank C. (2007). Fast and effective feature-preserving mesh denoising. *Visualization and Computer Graphics, IEEE Transactions on, 13*(5), 925-938.

Takasao, T, Shiiba, M, & Kitamura, H. (1976). *A distributed runoff model and lumping scale of a river basin.* Paper presented at the Proc. 31st Annu. Conf. JSCE.

Takasao, Takuma, & Shiiba, Michiharu. (1988). Incorporation of the effect of concentration of flow into the kinematic wave equations and its applications to runoff system lumping. *Journal of Hydrology, 102*(1), 301-322.

Tarekegn , Tesfaye H, & Sayama, Takahiro. (2013). Correction of SRTM DEM artefacts by fourier transform for flood inundation modeling. *Journal of Japan Society of Civil Engineers, Ser. B1 (Hydraulic Engineering), 69*(4), I_193-I_198.

Taubin, Gabriel. (1995). *A signal processing approach to fair surface design.* Paper presented at the Proceedings of the 22nd annual conference on Computer graphics and interactive techniques.

Tarekegn, Tesfaye Haimanot, Haile, Alemseged Tamiru, Rientjes, Tom, Reggiani, P, & Alkema, Dinand. (2010). Assessment of an ASTER-generated DEM for 2D hydrodynamic flood modeling. *International Journal of Applied Earth Observation and Geoinformation, 12*(6), 457-465.

UNESCAP. (2013). Statistical Year for Asia and the Pacific 2012; Website:

http://www.unescap.org/stat/data/syb2013/F.5-Natural-disasters.asp

Varley, P. (1994). Disaster, Development and the Environment,

(Chichester, UK: Wiley and Sons).

Vaze, Jai, Teng, Jin, & Spencer, Georgina. (2010). Impact of DEM accuracy and resolution on topographic indices. *Environmental Modelling & Software, 25*(10), 1086-1098.

Vollmer, Jörg, Mencl, Robert, & Mueller, Heinrich. (1999). *Improved laplacian smoothing of noisy surface meshes.* Paper presented at the Computer Graphics Forum.

Western, Andrew W, Grayson, Rodger B, & Blöschl, Günter. (2002). Scaling of soil moisture: A

hydrologic perspective. *Annual Review of Earth and Planetary Sciences, 30*(1), 149-180.

22 March. Available at http://www.worldwaterforum.net